HHS Public Access

Author manuscript

Dev Cell. Author manuscript; available in PMC 2018 July 10.

Published in final edited form as:

Dev Cell. 2017 July 10; 42(1): 22–36.e12. doi:10.1016/j.devcel.2017.05.016.

The CEP19-RABL2 GTPase complex binds IFT-B to initiate intraflagellar transport at the ciliary base

Tomoharu Kanie[1], **Keene Louis Abbott**[1], **Nancie Ann Mooney**[1], **Edward Douglas Plowey**[2], **Janos Demeter**[1], and **Peter Kent Jackson**[1,3,*]

[1]Baxter Laboratory, Department of Microbiology & Immunology and Department of Pathology, Stanford University School of Medicine, Stanford, CA 94305, USA

[2]Department of Pathology, Stanford University School of Medicine, Stanford, CA 94305, USA

Summary

Highly conserved intraflagellar transport (IFT) protein complexes direct both the assembly of primary cilia and the trafficking of signaling molecules. IFT complexes initially accumulate at the base of the cilium, and periodically enter the cilium suggesting a yet identified mechanism that triggers ciliary entry of IFT complexes. Using AP-MS purification of interactors of the centrosomal and ciliopathy protein, CEP19, we identify CEP350, FOP and the RABL2 GTPase as proteins organizing the first known mechanism directing ciliary entry of IFT complexes. We discover that CEP19 is recruited to the ciliary base by the centriolar CEP350/FOP complex, and then specifically captures GTP-bound RABL2B, which is activated via its intrinsic nucleotide exchange. Activated RABL2B then captures and releases its single effector, the intraflagellar transport B holocomplex, from the large pool of pre-docked IFT-B complexes and thus initiates ciliary entry of IFT.

eTOC Blurb

Intraflagellar transport protein (IFT) complexes accumulate at the ciliary base and periodically enter the cilium via an unknown mechanism. Kanie et al. show that CEP19 recruits the RABL2B GTPase complex to the ciliary base where it mediates release of IFT-B from pre-docked complexes to initiate IFT ciliary entry.

[*]To whom correspondence should be addressed. pjackson@stanford.edu.

[3]Lead contact

Author Contributions

Conceptualization, T.K. and P.K.J.; Methodology, T.K., K.L.A, and P.K.J.; Investigation, T.K., K.L.A., N.A.M., E.D.P, and J.D.; Writing – Original Draft, T.K. and P.K.J.; Writing – Review & Editing, T.K., K.L.A., and P.K.J.; Funding Acquisition, P.K.J.; Resources, P.K.J.; Supervision, T.K., and P.K.J.

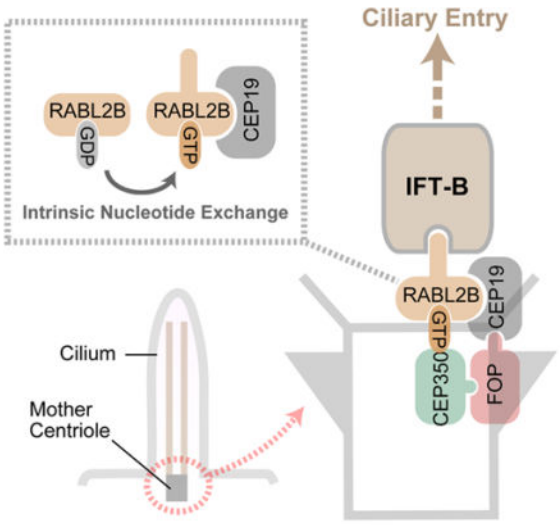

Introduction

Cilia and flagella are evolutionarily conserved organelles with important motile and sensory functions. The primary, or immotile, cilium is found on almost all cell types in the human body, and senses extracellular signals including hormones and morphogens (Ishikawa and Marshall, 2011). Defects in the formation or function of cilia cause a variety of disorders, called ciliopathies, which result in clinical phenotypes including retinal degeneration and obesity (reviewed in (Waters and Beales, 2011)). Structurally, cilia consist of nine microtubule doublets that form the axoneme, surrounded by a ciliary membrane. Since cilia lack protein synthesis machinery, their generation (ciliogenesis) largely relies on the delivery of ciliary proteins from the cytoplasm into the cilium (Pedersen and Rosenbaum, 2008). This active protein transport process is called intraflagellar transport (IFT). IFT is mediated by two large, highly-conserved protein complexes, IFT-A and IFT-B, and motor proteins. Ciliary cargo proteins are transported from the base to the tip by anterograde trains, powered by kinesin II. Cargos are then transported from the tip to the base by retrograde trains, directed by cytoplasmic dynein II (Pedersen and Rosenbaum, 2008; Taschner and Lorentzen, 2016). Defects in IFT-B typically cause severe ciliation defects, often leading to the absence of the cilium in various organisms including humans and *Chlamydomonas* (reviewed in (Pedersen and Rosenbaum, 2008), see Section 9) and embryonic lethality in mice (Bangs and Anderson, 2016), emphasizing the evolutionarily conserved role and essentiality of IFT-B in ciliogenesis.

Despite its initial purification from isolated *Chlamydomonas* flagella, immunofluorescence indicates the predominant localization of IFT components and motor proteins is at the ciliary base (Cole et al., 1998; Pazour et al., 1999), or more precisely at the transition fiber/distal appendage at the apical end of the centriole (Deane et al., 2001). IFT trains periodically enter into the cilium from this large pool of IFT particles located at the base (Dentler, 2005), and it has been long hypothesized that regulatory components accumulate at the ciliary base

to initiate anterograde IFT (Pedersen and Rosenbaum, 2008; Rosenbaum and Witman, 2002). To date, no critical regulator for the initiation of IFT has been identified.

Here, by tandem affinity purification and mass spectrometry of CEP19, we discover two interlinked protein complexes that trigger the entry of IFT into the cilium: the FOP-CEP350 and the CEP19 complex with the highly conserved RABL2B GTPase. CEP19 was first discovered by centrosomal proteomics as a novel protein (called C3orf34) localized specifically to the distal end of the mother centriole (Jakobsen et al., 2011). Recently, human morbid obesity patients were identified carrying a homozygous nonsense mutation (R82X) in CEP19. Mice deficient in CEP19 also exhibited hyperphagia and obesity (Shalata et al., 2013). In addition to obesity, human patients displayed a decreased sperm count resulting in male infertility, as well as intellectual disability (Shalata et al., 2013), similar to patients with Bardet-Biedl Syndrome, a ciliopathy syndrome marked by obesity, sterility, polydactyly, intellectual disability, and retinal degeneration (Forsythe and Beales, 2013).

We discover that CEP19 specifically binds to and is tethered at the base of cilia by the centriolar proteins CEP350 and FOP. We further find that CEP19 makes a stoichiometric complex with the highly conserved RABL2B GTPase, and serves to recruit RABL2B to the centriole. RABL2 binds GTP via its high, guanine-nucleotide exchange factor (GEF) independent nucleotide exchange activity. GTP-bound RABL2 then binds to the IFT-B holocomplex via the IFT74/81 heterodimer to capture and trigger the entry of IFT-B into cilia, prior to classical motor-driven intraflagellar transport. The CEP19-RABL2B-IFT pathway thus provides a new molecular mechanism directing ciliary trafficking and important for the formation of the cilium.

Results

Identification of RABL2-CEP19-FOP-CEP350 complexes

A recent report demonstrated that the monogenic obesity gene product CEP19 localizes to the base of cilia and its deficiency results in obesity and sperm motility defects, phenotypes characteristic of ciliary defects (Shalata et al., 2013). To better understand the function of CEP19, we constructed a LAP-CEP19 fusion stably expressed in retinal pigmented epithelial (RPE) cells, and used tandem affinity purification and mass spectrometry (Torres et al., 2009) to identify new CEP19 interacting partners. Visualizing these interacting proteins by silver staining SDS-polyacrylamide gels revealed a number of efficient, potentially stoichiometrically-interacting proteins (Fig. 1A). Mass spectrometry identified a number of specific, high efficiency interactions including the proteins RABL2B, FGFR1OP (FOP), and CEP350 (Fig. 1B). Interestingly, each of these four proteins are coordinately and strongly conserved in ciliated organisms, but not in non-ciliated organisms, suggesting the essential role of this complex in cilium formation or function (Fig S1A).

Rab-like protein 2 (RABL2) is a small GTPase not belonging to any subfamily within the small GTPase superfamily (Diekmann et al., 2011), but is thought to be an ancestral GTPase that exists in the last eukaryotic common ancestor (Elias et al., 2016). Although Rab-like proteins (RABL2-6) have little sequence similarity, two out of five RABL proteins, RABL4/IFT27 and RABL5/IFT22, are highly conserved components of the IFT-B complex. Humans

have two highly similar paralogs, RABL2A and RABL2B, which diverged after the split between humans and orangutans (Martin et al., 2002), with only three amino acid disparities (Wong et al., 1999). No functional differences have been reported. Recently, RABL2 was identified as an essential gene for sperm function. *Mot* mutant mice carrying a RABL2 D73G mutation exhibit sperm motility defects resulting in male infertility (Lo et al., 2012). The same group found that the *Mot* mutant mice, as well as *Rabl2* knockout mice, become obese (Yi Lo et al., 2016). The CEP350-FOP complex was first described as machinery that anchors microtubules to the centrosome (Yan et al., 2006), and recent papers have demonstrated that FOP has an important role in ciliogenesis (Lee and Stearns, 2013).

Validation of CEP350, FOP, CEP19, and RABL2B interactions indicates two distinct biochemical complexes

We confirmed direct biochemical interactions and determined the order of these interactions by using biochemical pull-downs with purified GST fusions of RABL2B, CEP19, and FOP (see Fig. S1B) mixed with *in vitro* translated MYC-tagged proteins of each potential partner. As shown before (Yan et al., 2006), FOP directly bound CEP350 C-terminal fragments, confirming this interaction (Fig. S1C, S1D, and S1E). CEP350 fragments did not bind CEP19, nor RABL2B. FOP efficiently bound GST-CEP19 (Fig. 1C), but not RABL2B (Fig. 1D). GST-CEP19 bound to full-length RABL2B and also to a fragment containing the GTPase domain (Fig. 1C); none of these proteins bound the GST control (Fig. 1E and S1D). Thus, the CEP19 interacting proteins associate in a direct and surprisingly linear manner from CEP350 and FOP binding to CEP19 and from CEP19 to RABL2B (Fig. 1F). Biochemical purification of the CEP19 complex demonstrates that a stable CEP19-RABL2B subcomplex can form (Fig. 1C) and a previous study (Yan et al., 2006), confirmed here (Fig. S1D), emphasize the FOP-CEP350 complex, suggesting the two subcomplexes exist, and that these complexes can interact somewhat efficiently in cells.

Localization of CEP19 and RABL2B to a compartment linked to the inner pericentriolar material

We next sought to understand where the individual components of the CEP19-RABL2 and CEP350-FOP subcomplexes localize and function. Using antibodies to endogenous CEP350 and FOP, we observed localization of each protein to both mother and daughter centrioles (Fig. 2A). Endogenous CEP19 localized only to the mother centriole as previously described (Jakobsen et al., 2011) (Shalata et al., 2013). Both a GFP-RABL2B fusion (Fig. 2A) and endogenous RABL2B (Fig. S2A) localized to the mother centriole and cytoplasm. Our RABL2B antibody exhibited high background staining, and since GFP-RABL2B equivalently localized to the mother centriole, it was used for the subsequent localization studies. In RPE cells, ciliation is exquisitely dependent on serum withdrawal. Examination of localization of these four proteins in RPE cells revealed that CEP19 and RABL2B are recruited to the centriole upon serum withdrawal, with RABL2B showing the most dramatic, switch-like serum dependence (Fig. 2A).

To better understand the localization of the CEP19 pathway components, we employed structured illumination microscopy (SIM). To first pinpoint CEP350 and FOP localization, we analyzed SIM images of endogenous CEP350 and FOP compared to GFP-tagged

CEP164, a marker of the distal appendage, and CEP170 or ninein, markers of the subdistal appendage and proximal end of the mother centriole (Sonnen et al., 2012). GFP-CEP164 colocalized with other previously identified distal appendage components (Tanos et al., 2013) (Fig. S2B), confirming that addition of a GFP-tag does not disrupt proper GFP-CEP164 localization to the distal appendage. We found CEP350 and FOP localized to an axial position on the mother centriole similar to the subdistal appendage marker CEP170, but displaced inwardly (Fig. 2B and 2C). In contrast, CEP19 and RABL2B each localized slightly apical to the subdistal appendage, but below the distal appendage (Fig. 2D and 2E). To confirm this localization, we analyzed the radial diameters of the 9-fold symmetric ring-like structure of CEP19. Consistent with a previous report (Sonnen et al., 2012), the diameter of the ring of inner pericentriolar material (inner PCM) protein CEP350 was significantly smaller than that of distal appendage protein, CEP164 (Table 1). The diameters of FOP, CEP19, and RABL2B rings were also significantly smaller than the CEP164 ring, similar to the diameter of the CEP350 ring (Table 1), suggesting that CEP19/RABL2B localizes most likely to the inner PCM (Fig. 2F, right). However, we could not exclude the possibility that CEP19/RABL2B could reside within a compartment in the most proximal portion of the distal appendage (Fig. 2F, left). Further study may help refine these two localizations.

To next determine the order of recruitment of these four components, we constructed sgRNA/Cas9-directed knockouts of CEP350, FOP, and CEP19, and a directed double knockout of RABL2A and RABL2B. Knockouts were confirmed by immunofluorescence or immunoblot (Fig. S3B and S3C). Using these lines, we observed that CEP350 and FOP were co-dependent in their recruitment to the mother and daughter centrioles and co-required to recruit both CEP19 and RABL2B to the mother centriole, although CEP350 knockouts showed a small amount of residual FOP and CEP19 localization (Fig. 2G and S2C–F). CEP19 was required for RABL2B recruitment, but had no effect on CEP350 or FOP localization (Fig. 2G). We confirmed that the absence of RABL2B at the base of cilia is not attributable to destabilization of the protein (Fig. S2G). RABL2A/B knockout had no effect on localization of the other components (Fig. 2G). Thus, the order of recruitment for proteins (CEP350/FOP-CEP19-RABL2B) closely paralleled the order of protein-protein interactions with CEP19 and RABL2B being targeted to the ciliary base via the CEP350-FOP complex (Fig. 1F and 2H).

CEP350, FOP, CEP19 and RABL2B are important for efficient and rapid ciliation

Mother centriole-specific localization of CEP19 and RABL2B and conservation of CEP350/FOP/CEP19/RABL2B components suggest that this pathway may be important for cilium formation, so we first tested CEP350, FOP, CEP19 and double mutant RABL2A/B RPE knockout cells for defects in ciliation. Following serum withdrawal (for 24 hours in this experiment), we assayed ciliation and observed that FOP knockout almost completely ablated ciliation, similar to knockout of CEP164, a critical distal appendage protein (Fig. 3A and S3A). CEP19 (Fig. 3A and S3A) and RABL2B (Fig. 3B) knockouts each showed a small percentage of residual ciliation and 33% of CEP350 knockout cells were ciliated (Fig. 3B). Using kinetic analysis of ciliation we observed that each of the knockout lines, with the exception of CEP350, displayed a notable delay in initiating ciliation and a substantial

reduction in the overall efficiency of ciliation (Fig. 3C). The mild phenotype of CEP350 knockout cells appears to be linked to the residual localization of FOP at the centrioles (Fig. 2G). The length of cilia in CEP19/RABL2 knockout cells are shorter than control cells at an early time point (24 hours), but comparable to control cells at a later time point (96 hours) with a significant increase in the number of cells with a long cilium (>5 μm) (Fig. S3D). Importantly, the mild but significant ciliation defect (40% ciliated cells at 48 hours serum starvation) in CEP19 knockout cells is not in perfect agreement with the previous study, which reported no observed ciliation defect at 48 hours post serum starvation in mouse embryonic fibroblasts (MEFs) deficient in CEP19 (Shalata et al., 2013). This difference might simply arise from differences between RPE cells and MEFs. Kinetic analysis of ciliation in CEP19 knockout MEFs may better assess the requirement of Rabl2 for ciliation in MEFs.

To establish the importance of CEP19 in ciliation, we rescued the CEP19 knockout defect by expression of untagged, wild type CEP19 (Fig. 3D). The R82X disease allele failed to rescue, confirming that the R82X allele is likely a null mutation and supporting a likely defect in ciliation in the original patient (Shalata et al., 2013). Expression of FOP (Fig. 3E) or RABL2B (discussed later and shown in Fig. 4B) each rescued ciliation in their respective knockout cells. RABL2A and RABL2B rescue the ciliation defect of RABL2A/B double knockout cells equivalently, suggesting that the two diverged genes are functionally redundant. We focused on RABL2B for further analysis because the expression level of RABL2B is dominant in various human tissues (Kramer et al., 2010).

A critical mechanistic switch for ciliation is the activation of the TTBK2 kinase, which plays an essential role in displacing the inhibitory CP110 protein from the mother centriole (Goetz et al., 2012). Examining our knockout cell lines, we found that CEP350 is required for recruitment of TTBK2 (Fig. 3F, upper panel) and displacement of CP110 (Fig. 3H), similar to the known role of CEP164 (Cajanek and Nigg, 2014) (Fig. 3G). FOP is partially important for recruiting TTBK2 (Fig. 3F) and displacing CP110 (Fig. 3G), presumably because of its importance in the proper localization of CEP350 to the centriole (Fig. 2H). Thus, TTBK2 recruitment and CP110 displacement leading to ciliation is downstream of CEP350 and works in parallel with CEP164, which directly binds and recruits TTBK2 (Cajanek and Nigg, 2014).

In contrast, we found that CEP19 and RABL2B are not important for regulating CP110 displacement or TTBK2 recruitment (Figs. 3F, 3G and 3H), even though both proteins are important for efficient ciliation. This phenotype is reminiscent of *Kif3a*$^{-/-}$ and *Ift88*$^{-/-}$ cells in which CP110 removal is intact but ciliation is severely affected due to deficiency of IFT(Goetz et al., 2012).

RABL2 uses a high turnover GTPase cycle to facilitate a GTP-specific activity critical for localization to the centriole and for ciliation

Given the importance of RABL2B in cilium formation and its highly conserved G1-G5 GTPase domains (Elias et al., 2016), we hypothesized that RABL2B engages in a conserved GTPase cycle critical for cilium assembly. To understand the RABL2B GTPase cycle, we first constructed classical alleles disrupting the GTPase and exchange activities. Mutation of

a highly conserved serine (S35N in RABL2B) required for magnesium binding in the P-loop reduces the affinity for guanine nucleotide, especially GTP. This mutation thus locks RABL2B in a GDP-bound or nucleotide-free state. Mutation of the highly conserved catalytic glutamine (Q80L in RABL2B) disrupts GTP hydrolysis, thus creating a GTP-locked state that strongly binds to effectors (Lee et al., 2009).

We first tested if the localization of RABL2B was affected by its guanine nucleotide state. First, wild type (WT) RABL2B efficiently localized to the base of the cilium upon serum withdrawal (~70%; Fig. 2A). RABL2B S35N completely failed to localize to the base of the cilium (Fig. 4A), indicating that GTP loading is required for recruitment of RABL2B to the centriole. Importantly, RABL2B Q80L localized at the ciliary base and accumulated within the cilium and at the tip in specific puncta, similar to that observed for IFT particles. As this trafficking pattern was never observed in the WT protein, we suggest that this is a result of the failure of the GTP-locked allele to turnover GTP and release from IFT. Broadly, the localization of WT RABL2B is consistent with a model wherein RABL2B undergoes GTP exchange to be recruited to the ciliary base and then GTP hydrolysis to release effectors at the ciliary base. Upon GTP hydrolysis, RABL2B would exit the ciliary base to be ready for the next GTP cycle.

The expression of GDP-locked RABL2A/B failed to rescue the ciliation defect of cells deficient of both RABL2A/B (Fig. 4B), supporting that GTP binding of RABL2B is indispensable for its role in cilium formation. In contrast, WT or GTP-locked RABL2A/B equally rescued the ciliation defect of RABL2 knockout, suggesting that GTP hydrolysis of RABL2 is not critical for ciliogenesis, at least when RABL2 is overexpressed (we observe ~15-fold excess relative to endogenous RABL2, Fig 4B). The efficient ciliation in the cells expressing GTP-locked RABL2B do not come from a defect in ciliary disassembly (Fig. S4A). We did observe the accumulation of BBSome component BBS4 and the ciliary GPCR GPR161 in cells expressing GTP-locked RABL2B, but not in the wild type or GDP-locked RABL2B expressing cells (Fig. S4B and S4C), suggesting that failure to release effector proteins at ciliary base could affect ciliary trafficking of components important for signaling. The mechanism that causes this change is currently unknown.

How does RABL2B become activated at the ciliary base? Canonical small GTPases bind to guanine nucleotide strongly with nM to pM dissociation constants, and require a GEF to lower the affinity for guanine nucleotide and activate effector binding to the GTPase (Bos et al., 2007). Because CEP19 directly binds RABL2B (Fig. 1C), we considered whether CEP19 might act as a GEF for RABL2B or serve another role upstream of RABL2B in addition to the recruitment of RABL2B. In agreement with this idea, overexpression of the GTP-locked form (Q80L) of RABL2B efficiently bypassed the ciliation defect of CEP19 and FOP knockout cells (Fig. 4C and S4D), while wild type RABL2B had weaker bypass activity and the GDP-locked form failed to rescue. Furthermore, the GTP-locked form of RABL2B localized to the ciliary base in CEP19 knockout and wild type cells, whereas wild type RABL2B failed to localize in CEP19 knockout cells (Fig. 4D). These observations support that CEP19 is involved in both the recruitment and GTP activation of RABL2B.

We next tested whether CEP19 could directly stimulate the nucleotide exchange of RABL2B *in vitro*. Here we used an exchange assay monitoring the loss of binding of a pre-loaded fluorescent MANT-GDP nucleotide upon the addition of excess non-hydrolyzable GTP, GppNHp. For this assay, we used *Chlamydomonas reinhardtii* Rabl2 (*Cr*Rabl2) because we found the interaction between RABL2 and CEP19 is conserved in *Chlamydomonas* (Fig. 4G), and *Cr*Rabl2 loaded MANT-GDP somewhat more efficiently than human RABL2B (Fig. S4E). Notably, purified *Cr*Rabl2 exhibited high intrinsic GDP/GTP exchange (k_{obs}=0.0028 S^{-1}, Fig. 4E), with little or no enhancement of nucleotide exchange by adding stoichiometric amounts of CEP19 (k_{obs}=0.0034 S^{-1}, Fig. 4E). This exchange rate is considerably higher than that of a traditional GEF-dependent GTPase like CDC42 (Fig. S4F, red), and is more consistent with rapid GEF-independent exchange, seen for example in the IIGP1 GTPase (Uthaiah et al., 2003) (Fig. S4G). We therefore suggest that RABL2 is an example of the class of GEF-independent GTPases (see discussion). Typically, GEF-independent GTPases rapidly exchange guanine nucleotide without a GEF because of their low μM affinity for GDP or GTP (Gasper et al., 2009). Fulfilling an additional criterion that RABL2 is GEF-independent, we found that its affinity for MANT-GDP or MANT-GTPγS (a GTP mimetic) was 1.3–1.4 μM (Fig. 4F), similarly to reported equilibrium dissociation constant of IIGP1 (0.9–1.0 μM for MANT-GDP) (Uthaiah et al., 2003).

To further understand the role of CEP19's interaction with RABL2, we reconstituted the interaction of purified GST-CEP19 with *in vitro* translated RABL2 in the presence of GTP or GDP with both human and *Chlamydomonas* proteins (Fig. 4G and S4H). GTP addition strongly enhanced RABL2 binding to CEP19 (5-fold), whereas GDP addition partially blocked RABL2 interaction with CEP19 (Fig. 4G and S4H). Neither the GTP-locked nor GDP-locked mutants of RABL2 measurably bound to CEP19 both *in vitro* (Fig. 4G and S4H) and *in vivo* (Fig. S4I). As we show in the next section, GTP-locked RABL2B efficiently bound its key effector, so CEP19 also does not appear to bind RABL2 as a traditional effector. Specifically, we suggest that CEP19 may interact with the nucleotide binding surfaces of RABL2 such that the GDP- or GTP-locked mutations disrupt binding to CEP19. In sum, we propose that RABL2 binds to GTP via its intrinsic nucleotide exchange activity and the activated GTP-bound RABL2 is preferentially recruited to the ciliary base by CEP19 (Fig. 4H, also see discussion). We next sought to identify RABL2B's key effector.

Purification of the GTP-locked form of RABL2B identifies IFT-B as a key effector

To better understand the role of RABL2B in controlling ciliation, we performed tandem affinity purifications of LAPN-RABL2B WT, Q80L, and S35N. Purified RABL2B variants were resolved by SDS-PAGE and silver staining revealed a distinctive pattern of protein bands specific to the Q80L allele (Fig. 5A). Mass spectrometry revealed that all 17 known components of the IFT-B complex were the top and almost exclusive hits in the purification with overall very high efficiency of copurification (Fig. 5B and Table S1). We ran a LAPC-IFT88 purification side-by-side with the RABL2B Q80L purification to emphasize similarities. Both RABL2A and RABL2B equally bound to IFT-B (Fig. S5A). SIM revealed that IFT88 almost perfectly colocalized with RABL2B at the ciliary base (Fig. 5E) with a diameter similar to that of inner PCM proteins (Fig. S6I and Table 1). Thus, we propose that upon activation, RABL2B·GTP captures the IFT-B holocomplex at the ciliary base.

RABL2B binds to IFT-B1 via IFT74/81

Previous structural and biochemical work on the highly homologous *Chlamydomonas* IFT-B complex revealed two subcomplexes, denoted IFT-B1 (core) and IFT-B2 (peripheral) (Taschner et al., 2016). IFT52 is a critical bridge between the IFT-B1 to the IFT-B2 subcomplexes (Taschner et al., 2016), and also links two IFT-B1 subcomplexes (IFT81/74/22/27/25 and IFT88/70/52/46) (Taschner et al., 2014). An IFT52 variant bearing K127E and R195E mutations disrupts interaction of the IFT-B1 and IFT-B2 sub-complexes (Taschner et al., 2016), whereas a C-terminal fragment of IFT52 dissociates the IFT81/74/22/27/25/46/56 sub-complex from the IFT-B holocomplex (Taschner et al., 2014). We stably expressed each IFT52 variant in RPE cells to dissociate the IFT-B complex, and found that RABL2B Q80L binds to the IFT-B1 complex and even more selectively to the IFT81/74/22/27/25/46/56 subcomplex (Fig. 5C).

To define the specific interaction partner of RABL2B, we deleted components of the IFT-B1 subcomplex by sgRNA/Cas9 and tested which were required for IFT-B to bind RABL2B Q80L. The IFT-B complex in cells lacking IFT74 or IFT81, but not other components, failed to bind to RABL2B, suggesting that the IFT74/81 heterodimer is the interaction partner of RABL2B (Fig. 5D). Additional mapping revealed that RABL2B binds to the C-terminal portions of both IFT74 and IFT81, distinct from the N-terminal tubulin cargo binding domains of IFT74/81 (Fig. S5B).

CEP19-RABL2B complex does not affect stability, complex formation, or pre-recruitment of IFT-B, but FOP is critical for IFT-B pre-recruitment to centrioles

To gain insight into the biological significance of RABL2B's interaction with IFT-B, we first sought to define where this interaction occurs. SIM revealed that GTP-locked, but not WT, RABL2B co-localized with ciliary IFT-B particles (Fig. S6A and S6B), suggesting that RABL2B WT interacts with IFT-B only at the ciliary base. What does RABL2B do at the ciliary base? We first tested the hypothesis that the CEP19-RABL2B complex affects the stability, complex formation, or initial recruitment of IFT-B to the centriole. We tested each of these potential activities, and did not see any obvious difference between control and CEP19 or RABL2 knockout cells (Fig. 6A and S6C–H). Additionally, neither the precise localization (Fig. 6B) nor the ultrastructure of the IFT88 ring (Fig. S6I) were affected by loss of CEP19 or RABL2.

In contrast to CEP19/RABL2 knockout cells, CEP350 and FOP knockout cells failed to recruit IFT-B to the base of cilia (Fig. 6A and S6F–H). This loss of recruitment is similar to the loss of centriolar IFT-B in CEP164 knockout cells previously reported (Schmidt et al., 2012) and confirmed here (Fig. 6A and S6F). The loss of centriolar IFT-B in CEP350 or FOP knockout cells might partially come from the loss of TTBK2 (Fig. 3F), a key initiator of ciliation, which is also required to recruit IFT-B to the ciliary base (Goetz et al., 2012). We propose that IFT-B is first recruited to the inner PCM in a pre-recruitment step downstream of CEP350-FOP and upstream of CEP19-RABL2B. Future studies will focus on a more complete definition of the centriolar pre-recruitment anchor.

Stable knockout of CEP19 or RABL2 decreases the number of IFT-B trains undergoing anterograde and retrograde movement, with no effect on IFT velocities or processivity

Next, we tested the role of CEP19 and RABL2B in the post-recruitment step for IFT-B, namely the entry of IFT-B into the cilium. We developed an assay using SIM to count the number of ciliary IFT-B particles in the cilium (Fig. 6C). The ability of CEP19/RABL2 knockout cells to ciliate (Fig. 3C), albeit less efficiently than that of wildtype cells, allowed us to analyze IFT in cilia in those knockout cells. We immediately observed a clear deficit in the number of IFT-B particles in cilia adjacent to the axoneme (Fig. 6C, quantitation in 6D), suggesting that RABL2B promotes the entry of IFT-B particles into the cilium. Given that the number of the particles inside cilia is correlated with cilia length (Dentler, 2005), we excluded the possibility that this reduction in the number of IFT-B particles inside the cilium is due to differences in the length of the cilia we analyzed to count particles in control and knockout cells (Fig. S6J). A perturbation in the number of IFT-B particles in cilia might result from a failure of initial entry or an alteration in the rate of traffic or residence time. To address the effect of CEP19 and RABL2B on IFT, we filmed IFT in CEP19 and RABL2 knockout cells to observe the frequency and rate of anterograde and retrograde trafficking events. We observed a ~4–5-fold reduction in the number of IFT-B anterograde trafficking events in both knockout cells (Fig. 6E, 6F, and Movie S1), consistent with fewer IFT-B particles entering the cilium. As expected, we observed a similar reduction in the number of retrograde events at steady state, consistent with retrograde trafficking events being directly linked to anterograde trafficking events. In contrast, analysis of kymographs showed no alteration of the velocities of anterograde or retrograde trafficking, nor any changes in the duration or processivity of trafficking events (Fig. 6G), supporting that changes in the number of IFT-B particles in cilia are not based on transport or residence time, but instead on ciliary entry. Importantly, although the ciliary entry of IFT was significantly reduced in CEP19 and RABL2 knockout cells, 20–30% of IFT-B particles were still able to enter the cilium. Further studies are needed to explain whether IFT-B can enter the cilium without CEP19-RABL2B less efficiently, or if additional factors allow the slow assembly of cilia in CEP19 or RABL2 knockout cells. In sum, our data suggest that the CEP19-RABL2 GTPase complex initiates IFT-B entry into the cilium.

Rabl2 knockout mice present a characteristic ciliopathy phenotype

The importance of RABL2 in the formation of primary cilia implied that mice deficient in *Rabl2* might show phenotypes characteristic of ciliopathies, notably male infertility, obesity, polydactyly, and retinal degeneration. Indeed, the previously reported *Rabl2* mutant mice exhibited sperm motility defects and obesity (Lo et al., 2012; Yi Lo et al., 2016). We thought these mice could have additional phenotypes caused by primary cilia dysfunction, including polydactyly and retinal degeneration. To test this hypothesis, we obtained and analyzed the knockout mice. Strikingly, we observed pre-axial polydactyly in 6 out of 9 $Rabl2^{-/-}$ mice, but neither in 13 $Rabl2^{+/-}$ nor 10 $Rabl2^{+/+}$ littermates (Fig. 7A). In addition, all three 16-week-old $Rabl2^{-/-}$ mice analyzed showed retinal degeneration, characterized by loss of the outer nuclear layer that contains the cell body of photoreceptor cells (Fig. 7B). Wild type and heterozygous mice were normal. These results strongly suggest that the $Rabl2^{-/-}$ phenotype is likely caused by a global dysfunction of cilia, reminiscent of Bardet-Biedl syndrome, and that RABL2 functions not only in motile cilia, but also in primary cilia.

Discussion

We discovered that the CEP19-RABL2B complex functions as a critical regulator that initiates intraflagellar transport at the ciliary base. Here we present a model and potential steps towards ciliary entry of IFT-B (Fig. 7C). Upon serum withdrawal, IFT complexes are recruited to the ciliary base by an undefined centriolar anchor, which is potentially downstream of CEP164 and FOP. Concurrently, the CEP350-FOP complex promotes recruitment of both the CEP19-RABL2B complex and TTBK2 to the mother centriole. RABL2B binds GTP via its intrinsic nucleotide exchange activity, and the activated RABL2B is recruited to the ciliary base by CEP19. RABL2B then binds to IFT-B via the IFT74/81 heterodimer to initiate ciliary entry of IFT-B. Having now defined critical factors that initiate ciliary entry of IFT-B, we can now begin to consider other steps in the process of ciliary entry, the upstream regulation that initiates intraflagellar transport.

The role of RABL2B in ciliary entry of IFT-B

Although our data demonstrate that RABL2B initiates IFT-B entry into the cilium at the ciliary base, the steps subsequent to RABL2B binding IFT-B remain unknown. Following recruitment, IFT entry is believed to be initiated by assembly of IFT trains, cargo loading, and the association with motor proteins (Pedersen and Rosenbaum, 2008), although molecular mechanisms of each process are currently unknown. We explore here the possibility that RABL2B might be involved in any of these processes.

We consider first the assembly of IFT trains. Several lines of evidence, including electron tomographic analysis (Pigino et al., 2009) and immunogold scanning electron microscopy (Sloboda and Howard, 2007), suggested that each IFT train consists of multiple IFT particles. IFT particles from isolated *Chlamydomonas* flagella consist of both the IFT-A and IFT-B complexes (Cole et al., 1998). Together, these data suggest that each train contains multiple IFT-A and IFT-B complexes. Given that IFT trains travel along the axoneme with only occasional merges and few pauses (Dentler, 2005), the assembly of large IFT trains would presumably occur at the cilium base. A recent study revealed that the N-terminal region of IFT74 was required for the association of IFT-A and IFT-B (Brown et al., 2015). Mutant algae lacking this region displayed significantly reduced frequencies of both anterograde and retrograde IFT trains. IFT-B components accumulated at the tips of cilia, whereas IFT-A was unable to enter into the cilium, suggesting the loss of connection between IFT-A and IFT-B in the mutant algae (Brown et al., 2015).

Of interest here, RABL2 bound to the IFT-B complex via IFT74/81 (Fig. 5D). Further, in RABL2 knockout cells, the frequency of anterograde and retrograde IFT trains was significantly reduced (Fig. 6F), suggesting that RABL2 might promote the assembly of IFT trains via binding to IFT74. Although we did not observe accumulation of IFT-B components at the tips of cilia, this hypothesis needs to be tested in further studies. It is also possible that RABL2B is required for connecting a pair of IFT-A/IFT-B complexes to another pair to form larger IFT trains. Our data did not exclude the possibility that the reduced number of IFT trains in RABL2 knockout cells (Fig. 6C–E) is due to the failure of detecting smaller trains, which have lower fluorescent signal. This hypothesis warrants further study.

We next consider cargo loading. Cargo proteins are known to accumulate at the ciliary base (Pazour et al., 1999), where they are loaded onto IFT trains before entering the cilium. Tubulin is one of the rare ciliary proteins in which direct partnership with IFT has been shown *in vitro*: IFT74/81 bind tubulin via their N-terminal regions (Bhogaraju et al., 2013). Since RABL2B binds IFT-B via IFT74/81, RABL2B could promote the loading of tubulin or other cargos onto IFT74/81 and only IFT-B loaded with tubulin would enter the cilium. Although the "cargo loading to IFT initiation" model is quite intriguing, this model has some conflicts with previous observations. First, cargo transport increases dramatically in growing cilia (Craft et al., 2015; Wren et al., 2013), whereas the frequency of IFT is independent of the length of cilia (Dentler, 2005). Second, algae carrying either IFT81 or IFT74 mutants lacking their tubulin-binding domains have greatly reduced tubulin transport rates, but the frequency of anterograde IFT is not significantly affected (Kubo et al., 2016). Nonetheless the dynamic nature of the process necessitates careful kinetic analysis and these hypotheses will require additional detailed tests. Finally, we consider the association of the IFT complex with its motor protein, kinesin II. It would be intriguing to test whether RABL2 promotes the loading of IFT-B on its motor; however, the interaction between IFT and this motor is still controversial (reviewed in (Taschner and Lorentzen, 2016). Ideally, the interaction between IFT complexes and kinesin II would be confirmed *in vitro*, but super resolution microscopy may distinguish the IFT-bound kinesin and free kinesin, thus allowing us to test this hypothesis.

The GTPase cycle of RABL2B

Our results suggest that RABL2B is likely a GEF-independent small GTPase. Although most small GTPases require a GEF for nucleotide exchange, several GTPases undergo nucleotide exchange without a GEF (reviewed in (Gasper et al., 2009)). Typically, this class of GTPases belongs to G proteins activated by nucleotide-dependent dimerization (GADs) (Gasper et al., 2009). In addition to their low affinity for GDP/GTP, GADs also have high GTP hydrolyzing activity, enabling them to inactivate themselves in a GAP-independent manner. This self-GTP hydrolysis is achieved by dimerization, where one protomer complements and/or stabilizes the active site of the other protomer (Gasper et al., 2009). Our preliminary data showed that untagged human RABL2B forms a tetramer *in vitro* (data not shown), implying that it might also have high GTP hydrolyzing activity. In agreement with this, RABL2B appears to undergo rapid hydrolysis after it activates IFT-B at the base of the cilium (Fig. 4A and 6A). Interestingly, another Rab-like small GTPase, RABL4/IFT27, also has low affinity for guanine nucleotide (GDP: Kd=37 μM; GTP: Kd=19 μM), but exhibits very low GTP hydrolyzing activity (Bhogaraju et al., 2011). The difference between RABL2B and RABL4/IFT27 is supported by the biochemical data, in which both RABL4/IFT27 WT and GTP-locked can efficiently bind to the IFT-B complex (Liew et al., 2014), whereas only the GTP-locked form of RABL2B, not WT, can bind to IFT-B (Fig. 5A and 5B). Another interesting aspect of RABL2B is its relationship with CEP19. Our current model is that CEP19 binds to GTP-bound RABL2B more strongly, thus promoting accumulation of the active form of RABL2B at the ciliary base (Fig. 4H). CEP19 may instead inhibit the intrinsic GTP hydrolyzing activity of RABL2B in order to stabilize its binding to GTP. Supporting this hypothesis is the fact that GTP-bound, not GTP-locked, RABL2B binds to CEP19 (i.e. the catalytic glutamine of RABL2B might participate in the

binding surface between CEP19 and RABL2B). Further studies are needed to more clearly understand the GTPase cycle of RABL2B and how it may be regulated.

RABL2B and CEP19 are candidate causative genes for Bardet-Biedl Syndrome

We show here that *Rabl2*$^{-/-}$ mice develop retinal degeneration and polydactyly, in addition to the previously described sperm motility defects (Lo et al., 2012) and obesity (Yi Lo et al., 2016). To date, RABL2B mutations have not been found in human ciliopathy patients, possibly because of the existence of functionally similar paralogs in humans, RABL2A and RABL2B (Fig. 4B). Consistent with the link between RABL2B and CEP19 we described here, patients carrying CEP19 R82X also display obesity and male infertility (Shalata et al., 2013). These phenotypes are reminiscent of Bardet-Biedl syndrome (BBS). Importantly, this phenotype is evidently very different from strong IFT-B deficiencies, which typically cause early embryonic lethality. This difference can be explained by the difference of ciliation phenotype between RABL2/CEP19 knockout cells and IFT-B deficiency. Cilia are essentially absent in IFT-B knockout mice (reviewed in (Goetz and Anderson, 2010)), which is also true for protozoans (reviewed in (Pedersen and Rosenbaum, 2008), see Section 9), mouse embryonic fibroblasts (Ocbina and Anderson, 2008), and human RPE-hTERT cells (Katoh et al., 2017). In contrast, a substantial proportion of CEP19/RABL2 knockout can still form cilia (Fig. 3C), probably because IFT can still enter the cilium in CEP19/RABL2 knockout cells to some extent (Fig. 6F). Therefore, we did not find it surprising that the mouse phenotype more closely resembles an IFT88 hypomorph, which were born at Mendelian ratio, and exhibit polydactyly (Moyer et al., 1994) and retinal degeneration (Pazour et al., 2002). In IFT88 hypomorph mice (or Orpk mice), ciliation is partially but significantly affected in many tissues (Banizs et al., 2005; Cano et al., 2004; Pazour et al., 2000). Another possible explanation for the viability of *Rabl2*$^{-/-}$ mice is that RABL2 is dispensable for ciliation in the neural tube, as is the case of some ciliated organisms that have most of IFT components but lack RABL2 (e.g. *C. elegans* and *D. melanogaster*, see Fig S1A).

The pathophysiology of the phenotype of *Rabl2*$^{-/-}$ mice is also largely unknown. The phenotype might simply come from the partial inhibition of ciliation, or it might come from defects in the trafficking of ciliary signaling components. Exactly how IFT-B is involved in the trafficking of signaling components is still unclear, and must be tested in future studies.

STAR Methods

Contact for Reagent and Resource Sharing

Further information and requests for resources and reagents should be directed to and will be fulfilled by the Lead Contact, Peter Jackson (pjackson@stanford.edu).

Experimental Model and Subject Details

Mice—Rabl2$^{+/-}$ mice in a C57BL/6 background were generated by in vitro fertilization using the sperm carrying the Rabl2tm1.1(KOMP)Wtsi (MGI:5548568) allele, which was obtained from International Mouse Phenotyping Consortium (http://www.mousephenotype.org/). The construct resulted in the deletion of exons 3–8 of mouse

Rabl2. Additional phenotypes of these mice are available at http://www.mousephenotype.org/data/genes/MGI:1915958#section-associations All mice were maintained under specific pathogen-free conditions at the Stanford animal care facility. All experiments were approved by Administrative Panel on Laboratory Animal Care at Stanford University.

The primers used for genotyping PCR are F: 5′-TGGGCTTGGTAATGGTGATT-3′, WT-R: 5′-CTGTGAGGAGCCAGTGTGAA-3′, KO-R: 5′-GTACCCCAGGCTTCACTGAG-3′.

Cell line—RPE-hTERT cells and 293T cells were grown in DMEM/F-12 (12400024, Thermo Fisher Scientific) supplemented with 10% FBS (100–106, Gemini), 1×GlutaMax (35050-079, Thermo Fisher Scientific), 100 U/mL Penicillin-Streptomycin (15140163, Thermo Fisher Scientific) at 37°C in 5% CO2.

Method Details

Tandem affinity purification—5 mL packed cell volume of RPE-hTERT cells expressing LAP-tagged proteins were re-suspended with 20 mL of LAP-resuspension buffer (300 mM KCl, 50 mM HEPES-KOH [pH 7.4], 1 mM EGTA, 1 mM $MgCl_2$, 10% glycerol, 0.5 mM DTT, and protease inhibitors [PI88266, Thermo Scientific]), lysed by gradually adding 600 μL 10% NP-40 to a final concentration of 0.3%, then incubated on ice for 10 min. The lysate was first centrifuged at 14,000 rpm (27,000 g) at 4°C for 10 min, and the resulting supernatant was centrifuged at 43,000 rpm (100,000 g) for 1 hr at 4°C to further clarify the lysate. High speed supernatant was mixed with 500 μL of GFP-coupled beads (Torres et al., 2009) and rotated for 1 hr at 4°C to capture GFP-tagged proteins, and washed five times with 1 mL LAP200N buffer (200 mM KCl, 50 mM HEPES-KOH [pH 7.4], 1 mM EGTA, 1 mM $MgCl_2$, 10% glycerol, 0.5 mM DTT, protease inhibitors, and 0.05% NP40). After re-suspending the beads with 1 mL LAP200N buffer lacking DTT and protease inhibitors, the GFP-tag was cleaved by adding 5 μg of TEV protease and rotating tubes at 4°C overnight. All subsequent steps until the cutting of bands from protein gels were performed in a laminar flow hood. TEV-eluted supernatant was added to 100 μL of S-protein agarose (69704-3, EMD Millipore) to capture S-tagged protein. After washing three times with LAP200N buffer lacking DTT and twice with LAP100 buffer (100 mM KCl, 50 mM HEPES-KOH [pH 7.4], 1 mM EGTA, 1 mM $MgCl_2$, and 10% glycerol), purified protein complexes were eluted with 50 μL of 2X LDS buffer and boiled at 95°C for 3 min. Samples were then run on Bolt® Bis-Tris Plus Gels (NW04120BOX, Thermo Fisher Scientific) in Bolt® MES SDS Running Buffer (B000202, Thermo Fisher Scientific). Gels were fixed in 100 mL of fixing solution (50% methanol, 10% acetic acid in Optima™ LC/MS grade water [W6-1, Thermo Fisher Scientific]) at room temperature, and stained with Colloidal Blue Staining Kit (LC6025, Thermo Fisher Scientific). After the buffer was replaced with Optima™ water, the bands were cut into eight pieces, followed by washing twice with 500 μL of 50% acetonitrile in Optima™ water. The gel slices were then reduced and alkylated followed by destaining and in-gel digestion using 125 ng Trypsin/LysC (V5072, Promega) as previously described (Shevchenko et al., 2006) with the addition of Protease Max (V2071, Promega) to increase digestion efficiency. Tryptic peptides were extracted from the

gel bands and dried in a speed vac. Prior to LC-MS, each sample was reconstituted in 0.1% formic acid, 2% acetonitrile, and water. NanoAcquity (Waters) LC instrument was set at a flow rate of either 300 nL/min or 450 nL/min where mobile phase A was 0.2% formic acid in water and mobile phase B was 0.2% formic acid in acetonitrile. The analytical column was in-house pulled and packed using C18 Reprosil Pur 2.4 uM (Dr. Maisch) where the I.D. was 100 uM and the column length was 20–25 cm. Peptide pools were directly injected onto the analytical column in which linear gradients (4–40% B) were of either 80 or 120 min eluting peptides into the mass spectrometer. Either the Orbitrap Elite or Orbitrap Fusion mass spectrometers were used, where a top 15 or "fastest" MS/MS data acquisition was used, respectively. MS/MS was acquired using CID with a collisional energy of 32–35. In a typical analysis, RAW files were processed using Byonic (Protein Metrics) using 12 ppm mass accuracy limits for precursors and 0.4 Da mass accuracy limits for MS/MS spectra. MS/MS data was compared to an NCBI Genbank FASTA database containing all human proteomic isoforms with the exception of the tandem affinity bait construct sequence and common contaminant proteins. Spectral counts were assumed to have undergone fully specific proteolysis and allowing up to two missed cleavages per peptide. All data was filtered and presented at a 1% false discovery rate (Elias and Gygi, 2007). Post processing using in-house MatLab and Excel scripts was used to further process the data for gene ontological analyses.

Plasmids—pG-LAP6/puro vector (pCDNA5/TO/FRT/EGFP-TEV cleavage site-S tag-PreScission cleavage site/DEST) was created by inserting a PreScission Protease cleavage site into the pG-LAP1 vector (Torres et al., 2009), and replacing the selection cassette from hygromycin to puromycin resistance.

pWPXLd/LAP-N/puro/DEST vector was created by inserting EGFP-TEV cleavage site-S tag-PreScission cleavage site/DEST/puromycin resistance casette of pG-LAP6/puro vector into pWPXLd vector, a gift from Prof. Didier Trono (Addgene plasmid #12258). pWPXLd/LAP-C/puro/DEST vector was generated by inserting DEST/TEV cleavage site-S tag-PreScission cleavage site-EGFP/puromycin resistance cassette into pWPXLd vector. pWPXLd/FLAG-N/blast/DEST vector was created by inserting FLAG/DEST/blastcidin resistance cassette into pWPXLd vector.

pWPXLd/FLAG-C/blast/DEST vector was created by inserting DEST/FLAG/blastcidin resistance cassette into pWPXLd vector. pMCB306, a lenti-viral vector containing loxP-mU6-sgRNAs-puro resistance-EGFP-loxP cassette, and P293 Cas9-BFP were gifts from Prof. Michael Bassik (Stanford University). pCMV-VSV-G and pCMV-dR8.2 dvpr were gifts from Prof. Bob Weinberg (Addgene plasmid #8454 and #8455) (Stewart et al., 2003). pOG44 (V600520) was obtained from Thermo Fisher Scientific.

pCS2-N-terminal 6×MYC/DEST (used for in vitro translation) and pGEX6p/DEST (used for recombinant protein expression in bacteria) was described previously (Wright et al., 2011).

The Gateway entry vector for Homo sapiens CEP19 was a gift from Prof. Marc Vidal. Gateway entry vectors for *H. sapiens* RABL2A (HsCD00073874), RABL2B

(HsCD00044423), FGFR1OP (HsCD00045089), CEP350 (HsCD00399246), CDC42 (HsCD00000265) were obtained from Harvard Plasmid. STOP codons were added or removed by using BP recombination if necessary. A Gateway entry vector for *H. sapiens* IFT88 was obtained from Prof. Saikat Mukhopadhyay.

Gateway entry vectors for *H. sapiens* IFT52, IFT74, IFT80, IFT81, and M. musculus IIGP1 were created by BP recombination using pCMV-SPORT6-IFT52 (HsCD00339273, Harvard Plasmid), pDNR-LIB-IFT74 (HsCD00340259, Harvard Plasmid), pCMV-SPORT6-IFT74 (HsCD00339316), pCR4-TOPO-IFT80 (HsCD00341166, Harvard plasmid), pENTR223-IFT81 (HsCD00287837, Harvard Plasmid), the C-terminal fragment of IFT81, and pCMV-SPORT6-IIGP1 (MMM1013-202761355, Dharmacon) as templates. The C-terminal fragment of IFT81 was PCR-amplified using cDNA from RPE-hTERT cells as a template, and cloned into pCR-bluntII-TOPO vector using Zero Blunt® TOPO® PCR Cloning Kit (K280020, Thermo Fisher Scientific).

Gateway entry vectors for *Chlamydomonas reinhardtii* Rabl2 and Cep19 were created by BP recombination between pDONR221 and synthesized double stranded DNA (gBlocks Gene Fragment, IDT).

Gateway entry vectors carrying point mutations of RABL2A, RABL2B, *C. reinhardtii* Rabl2 and IFT52 were created using site-directed mutagenesis. Gateway entry vectors carrying truncation mutants of CEP19 (1-82 a.a.), RABL2B (15-186 a.a.), CEP350 (1-1078 a.a., 1079-2169 a.a., 2170-2836 a.a., 2837-3116 a.a., 2170-2469 a.a., 2470-2836 a.a., 2470-2636 a.a., and 2637-2836 a.a.), IFT52 (1-326 a.a. and 350-432 a.a.), IFT81 (1-258 a.a., 122-676 a.a., 259-456 a.a., and 457-676 a.a.), and IFT74 (1-351 a.a., 91-600 a.a., 352-600 a.a.) were created by using BP recombination between pDONR221 and PCR-amplified inserts.

N-terminally LAP (EGFP-TEV cleavage site-S tag-PreScission cleavage site)-tagged RABL2A (wild-type and mutants), RABL2B (wild-type and mutants), CEP164, IFT81 (wild-type and mutants), and IFT74 (wild-type and mutants) were generated by LR recombination between entry vectors described above and pWPXLd/LAP-N/puro/DEST.

Flp-In system compatible N-terminally LAP-tagged CEP19 was generated by LR recombination between CEP19 entry vector and pG-LAP6/puro.

C-terminally LAP (TEV cleavage site-S tag-PreScission cleavage site-EGFP)-tagged IFT88 and IFT80 were generated by LR recombination between the IFT88 and IFT80 entry vector described above and pWPXLd/LAP-C/puro/DEST.

N-terminally FLAG-tagged RABL2B (wild-type and mutants) and IFT52 mutants were generated by LR recombination between entry vectors described above and pWPXLd/FLAG-N/blast/DEST.

Untagged empty, FOP, CEP19 (wild-type and mutants), RABL2A (wild-type and mutants), and RABL2B (wild-type and mutants) were generated by LR recombination between entry vectors containing a STOP codon and the pWPXLd/FLAG-C/blast/DEST vector.

N-terminally MYC-tagged CEP350 fragments, FOP, RABL2B (wild-type and mutants), and *C. reinhardtii* Rabl2 (wild-type and mutants) were generated by LR recombination between entry vectors described above and pCS2-N-terminal 6×MYC/DEST.

N-terminally GST tagged FOP, CEP19, RABL2B, CDC42, KRAS2B, IIGP1, *C. reinhardtii* Rabl2, and *C. reinhardtii* CEP19 were generated by LR recombination between entry vectors described above and pGEX6p/DEST.

Lentiviral vectors containing sgRNAs were generated by ligating oligonucleotides encoding sgRNAs into the pMCB306 vector digested with BstXI and BlpI restriction enzymes.

Cell line generation—Cells were transfected with 3 μl (293T cells) or 6 μl (RPE cells) of Fugene 6 (E2692, Promega) and 1 μg of DNA.

RPE-FRT9 expressing LAP-CEP19 was generated by transfecting 150 ng of the preceding vectors with 850 ng of pOG44, followed by selection with 10 μg/ml puromycin. Flp-In system compatible RPE cells (RPE-FRT9) were previously described (Sang et al., 2011). All other stable cell lines were generated using lentivirus. Lentivirus carrying genes of interest were produced by co-transfecting 293T cells with 150 ng of pCMV-VSV-G, 350 ng of pCMV-dR8.2 dvpr, and 500 ng of pWPXLd or pMCB306 plasmids previously described. Media was replaced 24 hr after transfection to omit transfection reagent, and virus was harvested at 48 hr post-transfection. Virus was then filtered with a 0.45 μm PVDF filter (SLHV013SL, Millipore) and mixed with 4-fold volume of fresh media containing 12.5 μg/ml polybrene (TR-1003-G, Millipore). Following infection for 48–72 hr, cells were selected with either 10 μg/ml puromycin or 10 μg/ml blastcidin.

CRISPR knockout—RPE cells expressing BFP-Cas9 were generated by infection with lentivirus carrying p293 Cas9-BFP, followed by sorting BFP-positive cells using FACSaria (BD).

RPE-BFP-Cas9 cells were infected with lentivirus carrying sgRNAs in the pMCB306 vector to generate knockout cells. After selection with 10 μg/ml puromycin, cells were subjected to immunoblotting, immunofluorescence, or genomic PCR combined with TIDE analysis (Brinkman et al., 2014) to determine knockout efficiency. Cells were then infected with adenovirus carrying Cre-recombinase (1045, Vector BioLabs) at a multiplicity of infection of 50 to remove the sgRNA-puromycin resistance-EGFP cassette. 10 days after adenovirus infection, GFP-negative single cells were sorted using FACS Aria.

To exclude the possibility that the observed phenotypes of the knockout cells are due to off target effects, rescue experiments were performed by infecting knockout cells with lentivirus carrying untagged wild type genes of interest. Pools of knockout cells were created by mixing four single cell knockout clones of control (pMCB306 carrying sgGFP), FOP or CEP19, and two single cell knockout clones of CEP350 or RABL2.

The targeting sequences of guide RNAs are; CEP164: 5′-CTGCCTGGAGAGTGGAAAC-3′, CEP19: 5′-AGAACAAGTATCCCTGAGG-3′, RABL2A/B: 5′-AACCGAGTGAGTTGGAC-3′, FOP: 5′-

AGCAGCTGTGTTTTTAGCA-3′, CEP350: 5′-CAGGTGGTTCAATCACAAC-3′, IFT81: 5′-GTAATTTACCCAGTGCTC-3′, IFT74: 5′-ATCGCCCTGTAACACAA-3′, IFT22: 5′-AAAGCCAAGATCCTCTTCG-3′, IFT25: 5′-AAGTGATTTTAGCTACAT-3′, IFT27: 5′-AATGTCTTATGTCTCGT-3′, and IFT56: 5′-AAGAGGATACTAATTTG-3′.

Recombinant protein purification—pGEX6p vectors described above were transformed into Rosetta™ 2(DE3) pLysS bacteria cells (71403, EMD Millipore) and grown at 37°C until A600 reached 0.6–0.8. Protein expression was induced with 0.1 mM IPTG overnight at 18°C. Cells were harvested and re-suspended in bacterial lysis buffer (25 mM HEPES-NaOH [pH 7.4], 500 mM NaCl, 1 mM DTT, 5 mM $MgCl_2$, and 1% Triton X-100) with protease inhibitors (11873580001, Roche Applied Science), followed by sonication. The lysate was then clarified by centrifuging at 15,000 rpm (30,996 g). In order to purify GST-tagged proteins, the soluble fraction was mixed with Glutathione Sepharose 4B beads (17075605, GE healthcare) at 4°C for 2 hr, followed by washing three times with bacterial lysis buffer and twice with GST elution buffer (100 mM HEPES-NaOH [pH 8.0], 150 mM NaCl, 5 mM $MgCl_2$, and 40 mM reduced glutathione) without reduced glutathione. The GST-tagged proteins were then eluted in GST elution buffer at room temperature for 15 min, dialyzed in storage buffer (25 mM HEPES-NaOH [pH 7.4], 50 mM NaCl, 1 mM DTT, 5 mM $MgCl_2$, and 10% glycerol), concentrated with Amicon Ultra Centrifugal Filter Units (UFC801024, EMD Millipore), and stored at −80°C. To generate untagged proteins, proteins were washed twice with PreScission cleavage buffer (25 mM HEPES-NaOH [pH 7.4], 150 mM NaCl, 1 mM DTT, 5 mM $MgCl_2$, and 0.1% Triton X-100) instead of GST elution buffer. The GST-tag was cleaved overnight at 4°C in PreScission cleavage buffer with the addition of 2 μg of PreScission per 100 μg of recombinant protein, and the untagged proteins were dialyzed in storage buffer, concentrated, and stored at −80°C.

GST pull-down with in vitro translated protein—*In vitro* translated (IVT) proteins were generated with pCS2-N-terminal 6xMYC vectors previously described using TnT® SP6 High-Yield Wheat Germ Extract (L3260, Promega) and by following manufacturer's recommendations. For each pull-down reaction, 2.5 μg of GST or GST-tagged protein was added along with 1–10 μL IVT protein and 5 μL of washed Glutathione Sepharose 4B beads in 300 uL binding buffer (25 mM HEPES-NaOH [pH 7.4], 500 mM NaCl, 5 mM $MgCl_2$, and 0.1% Triton X-100) and mixed for 1 hr at 4°C. The beads were washed five times with the same buffer and eluted with LDS sample buffer. The eluates were then resolved by SDS-PAGE and analyzed by immunoblotting with anti-GST (G7781, Sigma-Aldrich) and anti-C-MYC (CBL430, EMD Millipore) antibodies. For pull-down assays using nucleotide-loaded IVT RABL2B, IVT RABL2B proteins were first generated as described above, then incubated at room temperature in the presence of 5 mM $MgCl_2$ and 1 mM GTP or GDP. The pull-down assays were performed as described with the loaded IVT proteins, with the exception that the binding buffer contained 1 mM GTP or GDP.

MANT-GDP loading assay—Recombinant proteins were first buffer exchanged into low magnesium buffer (20 mM HEPES-NaOH [pH 7.5], and 0.5 mM $MgCl_2$) using a NAP-5 column (1708531, GE Healthcare). The proteins (typically 30–100 μM) were then incubated with 20-fold molar excess of N-methylanthraniloyl (MANT)-GDP (69244, SIGMA) in

loading buffer (50 mM NaCl, 20 mM HEPES-NaOH [pH 7.5], 0.5 mM $MgCl_2$, 5 mM EDTA, and 1 mM DTT) in a total volume of 200 μl at 20°C for 90 min. The reaction was stopped by adding $MgCl_2$ to a final concentration of 10 mM, then incubated at 20°C for 30 min.

The free MANT nucleotide was removed using a NAP-5 column equilibrated with GEF reaction buffer (40 mM HEPES-NaOH [pH 7.5], 50 mM NaCl, 2 mM DTT, and 10 mM $MgCl_2$). MANT-bound proteins were loaded into a 384-well microplate (784076, Greiner), and the fluorescence was measured on a TECAN Infinite M1000 Microplate reader with an excitation wavelength of 360 ± 10 nm and emission wavelength of 440 ± 20 nm. The loading efficiency was calculated by using a standard curve of free MANT-GDP, and by estimating the signal goes up two-fold when it binds to the protein.

Guanine nucleotide exchange assay—Recombinant proteins were first loaded with MANT-GDP as described above then loaded into a 384-well microplate. The guanine nucleotide exchange reaction was initiated by adding 100-fold molar excess of non-hydrolyzable GTP analog, GppNHp (ab146659, Abcam), in the presence or the absence of *Hs*Dbs (GE01-A, Cytoskeleton) or CEP19. The decrease in fluorescence was monitored at room temperature every 15 seconds for at least 30 min on a TECAN Infinite M1000 Microplate reader. Occasionally, a spike in the fluorescent signal caused by reading error was observed, and was manually removed from the data. K_{obs} values were obtained by fitting the data to a single exponential function by using GraphPad Prism 7 software.

Measurement of equilibrium dissociation constant—Recombinant *Chlamydomonas reinhardtii* Rabl2 was titrated against 200 nM MANT-GDP or 200 nM slowly hydrolysable MANT-GTPγS (ab146758, Abcam) in 50 μl of GEF reaction buffer in a 96-well microplate (3686, Corning). After incubating for 1 hr at room temperature, fluorescence was measured on a TECAN Infinite M1000 Microplate reader. Equilibrium dissociation constant (Kd) was obtained by fitting a quadratic function to the data with the use of GraphPad Prism 7 software.

Antibody generation—To raise rabbit polyclonal antibodies against RABL2B and CEP19, bacterially purified untagged RABL2B (1-229 a.a.) and CEP19 (1-163 a.a.) were injected into rabbits (1 mg for first injection and 500 μg for boosts). The RABL2B antibody was affinity purified from the third serum bleed with the same antigen used for injection via standard protocols.

Immunofluorescence—For wide-field microscopy, cells were grown on 12 mm round coverslips and fixed with 4% paraformaldehyde (433689M, AlfaAesar) in phosphate buffered saline (PBS) for 10 min at room temperature. Cells stained with CEP89 or SCLT1 antibodies were fixed in 100% methanol for 5 min at −20°C. After blocking with 5% normal donkey serum (017-000-121, Jackson ImmunoResearch) in immunofluorescence (IF) buffer (3% BSA and 0.1% NP-40 in PBS) for 30 min at room temperature, cells were incubated with primary antibody in IF buffer for at least 2 hr at room temperature, followed by rinsing with IF buffer five times. The samples were then incubated with fluorescent-labeled secondary antibody in IF buffer for 1 hr at room temperature, followed by rinsing with IF

buffer five times. After nuclear staining with 4′,6-diamidino-2-phenylindole (DAPI) in PBS, coverslips were mounted with Fluoromount-G (0100-01, SouthernBiotech) onto glass slides. Images were acquired on an Everest deconvolution workstation (Intelligent Imaging Innovations) equipped with a Zeiss AxioImager Z1 microscope and a CoolSnapHQ cooled CCD camera (Roper Scientific). A 40x NA1.3 Plan-Apochromat objective lens (420762-9800, Zeiss) was used for ciliation assays, and a 63x NA1.4 Plan-Apochromat objective lens (420780-9900, Zeiss) was used for other analysis. At least 6 images from different fields per sample were captured for typical analysis.

For ciliation assays, cells were plated into a 6-well plate at a density of 2 x 10^5 cells/well and grown for 72 hr. Cells were serum starved for 24 hr unless otherwise indicated, and fixed in 4% paraformaldehyde (433689M, AlfaAesar). After the blocking step, cells were stained with anti-Arl13B, anti-CEP170, and anti-acetylated tubulin (Ac-Tub) antibodies, washed, then stained with anti-rabbit Alexa488, goat anti-mouse IgG1-Alexa568, and goat anti-mouse IgG2b Alexa647. The structures extending from the centrosome and positive for both acetylated tubulin and Arl13B were counted as primary cilia. Typically, at least 200 cells were analyzed per experiment.

For structured illumination microscopy, cells were grown on 18 mm square coverslips (474030-9000-000, Zeiss), fixed, and stained as described above. Coverslips were mounted with SlowFade Gold Antifade Reagent (S36936, Life Technologies). Images were acquired on a DeltaVision OMX V4 system equipped with a 100×/1.40 NA UPLANSAPO100XO objective lens (Olympus), and 488 nm (100 mW), 561 nm (100 mW), and 642 nm (300 mW) coherent sapphire solid state lasers, and Evolve 512 EMCCD cameras (Photometrics). Image stacks of 2 μm z-steps were taken in 0.125 μm increments. Images were then computationally reconstructed and subjected to image registration by using SoftWorx 6.5.1 software.

Primary antibodies used for immunofluorescence were anti-CEP350 (NB100-59811, NOVUS), anti-FOP (H00011116-M01, NOVUS), anti-RABL2B (affinity purified, in house), anti-CEP19 (26036-1-AP, Proteintech), anti-CEP19 (3rd bleed, in house), anti-CEP170 (41-3200, Thermo Fisher Scientific), anti-CEP164 (HPA037605, SIGMA), anti-SCLT1 (14875-1-AP, Proteintech), anti-FBF1 (HPA023677, SIGMA), anti-CEP89 (24002-1-AP, Proteintech), anti-acetylated tubulin (T7451, SIGMA), anti-GFP (A10262, Thermo Fisher Scientific), anti-IFT88 (13967-1-AP, Proteintech), anti-IFT81 (11744-1-AP, Proteintech), anti-IFT57 (11083-1-AP, Proteintech), anti-ARL13B (17711-1-AP, Proteintech), anti-BBS4 (12766-1-AP, Proteintech), and anti-GPR161 (Mukhopadhyay et al., 2013).

Secondary antibodies used for immunofluorescence were donkey anti-rabbit Alexa488 (711-545-152, Jackson ImmunoResearch), donkey anti-mouse IgG DyLight488 (715-485-150, Jackson ImmunoResearch), donkey anti-chicken IgY DyLight488 (703-485-155, Jackson ImmunoResearch), donkey anti-rabbit IgG Alexa568 (A10042, Thermo Fisher Scientific), goat anti-mouse IgG1-Alexa568 (A-21124, Thermo Fisher Scientific), goat anti-mouse IgG2b Alexa647 (A-21242, Thermo Fisher Scientific), donkey anti-rabbit IgG Alexa647 (711-605-152, Jackson ImmunoResearch), and donkey anti-mouse IgG Alexa647 (715-605-151, Jackson ImmunoResearch).

GFP co-immunoprecipitation—Cells were plated at a density of 1.5×10^6 cells per 15 cm dish or 0.5×10^6 cells per 10 cm dish, grown for 96 hr, serum starved for 24 hr. Cells were then lysed with NP-40 lysis buffer (50 mM Tris-HCl [pH7.5], 150 mM NaCl, and 0.3% NP-40, 10 μg/ml LPC (leupeptin, pepstatin A, and chymostatin), and 1% phosphatase inhibitor cocktail 2 (P5726, SIGMA) followed by clarification of the lysate by centrifugation at 15,000 rpm (21,000 g) for 10 min. The soluble fraction was incubated with GFP-coupled beads (Torres et al., 2009) (10 μl bed volume per 3 mg of lysate) for 1.5 hr at 4°C, followed by washing five times with IP wash buffer (50 mM Tris-HCl [pH 7.5], 150 mM NaCl, and 0.1% NP-40). Samples were eluted with 2 × LDS buffer containing 2.5% 2-mercaptoethanol (M3148, SIGMA).

Immunoblot—For immunoblotting, cells were lysed in NP-40 lysis buffer followed by clarification of the lysate by centrifugation at 15,000 rpm (21,000 g) for 10 min. Samples were then mixed with 2 × LDS buffer containing 2.5% 2-mercaptoethanol and incubated at 95°C for 5 min. Proteins were separated in NuPAGE™ Novex™ 4–12% Bis-Tris protein gels (WG1402BOX, Thermo Fisher Scientific) in NuPAGE™ MOPS SDS running buffer (50 mM MOPS, 50 mM Tris Base, 0.1% SDS, 1 mM EDTA, pH 7.7), then transferred onto Immobilon™-FL PVDF Transfer Membranes (IPFL00010, EMD Millipore) in Towbin Buffer (25 mM Tris, 192 mM glycine, pH 8.3). Membranes were incubated in LI-COR Odyssey Blocking Buffer (NC9232238, LI-COR) for 30 min at room temperature, then probed overnight at 4°C with the appropriate antibody diluted in blocking buffer. Next, membranes were washed 3 x 5 min in TBST buffer (20 mM Tris, 150 mM NaCl, 0.1% Tween 20, pH 7.5) at room temperature, incubated with the appropriate IRDye® antibodies (LI-COR) diluted in blocking buffer for 30 min at room temperature, then washed 3 x 5 min in TBST buffer. Membranes were scanned on an Odyssey CLx Imaging System (LI-COR) and proteins were detected at wavelengths 680 and 800 nm.

Primary antibodies used for immunoblot were anti-GFP (A11122, Invitrogen), anti-IFT81 (11744-1-AP, Proteintech), anti-IFT57 (11083-1-AP, Proteintech), anti-IFT25 (15732-1-AP, Proteintech), anti-IFT88 (13967-1-AP, Proteintech), anti-TTC30A (25352-1-AP, Proteintech), anti-IFT74 (NB300-822, NOVUS), anti-IFT22 (NBP1-84098, NOVUS), anti-CLUAP1 (17470-1-AP, Proteintech), anti-IFT27 (NBP1-87170, NOVUS), anti-TTC26 (25083-1-AP, Proteintech), anti-IFT140 (17460-1-AP, Proteintech), anti-CEP164 (22227-1-AP, Proteintech), anti-FOP (11343-1-AP, Proteintech), anti-RABL2B (affinity purified, in house), anti-FLAG (F7425, SIGMA), and anti-Secondary antibodies used for immunoblot were IRDye® 800CW donkey anti-mouse (926-32212, LI-COR), IRDye® 800CW donkey anti-rabbit (926-32213, LI-COR), IRDye® 680CW donkey anti-mouse (926-68072, LI-COR), and IRDye® 680CW donkey anti-rabbit (926-32223).

Live cell imaging—We initially used GFP tagged IFT88 for the live cell imaging, however, the expression of GFP-IFT88 completely inhibited the formation of the cilium in both CEP19 and RABL2 knockout cells. We screened for other IFT-B components, and found that only GFP-IFT80 worked in CEP19/RABL2 KO cells among seven IFT-B components tested (IFT20, 56, 70A, 38, 54, 57, and 80). We thus used GFP-IFT80 for this study.

RPE-BFP-Cas9, CEP19 knockout, and RABL2 knockout cells expressing C-terminally GFP tagged IFT80 were plated in an 8-well Lab-TekII Chambered Coverglass (155409, Thermo Fisher Scientific) at the density of 2×10^4 cells per well, grown for 72 hr, and serum starved for 48 hr. Live cell imaging was carried out on a DeltaVision OMX V4 system equipped with a 60×/1.49 NA APON60XOTIRF objective lens (Olympus), 488 nm (100 mW), 561 nm (100 mW), and 642 nm (300 mW) coherent sapphire solid state lasers, Evolve 512 EMCCD cameras (Photometrics), and TIRF system. Cells were imaged every 250 ms (4 fps) for 30 sec. Kymographs were created by using ImageJ with the KymoResliceWide plugin.

Histology—The right eye was enucleated from 16 week old *Rabl2*$^{-/-}$ mice (n=3, two females and one male), *Rabl2*$^{+/-}$ mice (n=3, two females and one male), and control *Rabl2*$^{+/+}$ littermates (n=2, one female and one male), and fixed in buffered formalin for three days. Eyes were then processed, embedded in paraffin blocks, and sectioned on a microtome (5 μm thick sections) by standard techniques. Hematoxylin and eosin sections were examined for evidence of photoreceptor degeneration. To quantify the extent of photoreceptor degeneration, 200x magnification images were obtained from the peripheral and posterior retinas from up to eight histologic sections of the central pupil-optic nerve axis. The averages of 27–48 linear measurements of the depths of the inner and outer nuclear layers were recorded for the peripheral and posterior retinas. The ratios of the inner and outer nuclear layer depths were compared with ANOVAs with posthoc Bonferroni pairwise comparisons (SYSTAT v13).

Phylogenetic analysis—To create Fig. S1A, Fig. 3 of (van Dam et al., 2013) were extended with data for FOP, FOPNL, RABL2, CEP19, and CEP350 along with orthology data from pantherdb, orthoMCL (PTHR15431 and OG5_133356, PTHR15431 and OG5_131172, PTHR24073:SF731 and OG5_132618, PTHR31539 and OG5_136689, PTHR13958 and OG5_134701, respectively). Since the rice and thale cress sequences aligned better with FOPNL (PTHR15431), orthology for these two genes reported in OG5_133356 was manually removed. Data from (Elias et al., 2016) for RABL2, in addition to the first 51 results of an NCBI BLAST search of the Nematostella vectensis sequences for FOP, CEP19, and CEP350 using default parameters, were used to identify additional orthologs to include in the table.

Quantification and Statistical Analysis

Measurement of the diameter of centriolar rings—The diameter of the rings formed by centrosomal proteins (Table 1 and Fig. S6I) was measured with images acquired by structured illumination microscopy. To measure the diameter of the ring, the distance between intensity maxima was measured from four different angles using top-view image and averaged to reduce the variability caused by tilting of the centriole.

Quantification of fluorescent intensity—The fluorescent intensity of centrosomal proteins was measured with 16-bit TIFF images acquired at 63x magnification by using Image J software. The minimum and maximum brightness of each analyzed channel was normalized without cutting off excessive signal. A rolling ball background subtraction with a rolling ball radius of twice the width (25 pixels) of the centriole (12.5 pixels) was then

implemented to reduce background intensity. To obtain the fluorescent intensity of the protein of interest (POI), a circle was placed surrounding the centriole (indicated by CEP170), and the integrated density of both CEP170 and the POI were measured. In order to reduce leaky signal from adjacent Z dimensions and the cytoplasm, the average intensity of three adjacent circles of the same size were subtracted from the CEP170 and POI integrated densities; any negative values were manually corrected to 0. The signal ratio of the POI over CEP170 were then normalized relative to the average signal ratio of control cells. Outliers were excluded using the ROUT method with a false discovery rate of 1% using GraphPad Prism 7 software.

For the fluorescent intensity of ciliary proteins shown in Fig. S4B and S4C, the signal of acetylated tubulin instead of CEP170 was used for a reference. Typically, 50–100 of cilia/centrosome were analyzed for each cell line. The result was confirmed in at least three independent experiments or three single cell clones.

Statistical analysis—Data were analyzed by unpaired two-tailed Student's t test unless otherwise indicated. Asterisks denote *: $0.01 \leq p < 0.05$, **: $p < 0.01$, ***: $p < 0.001$, n.s.: not significant.

Supplementary Material

Refer to Web version on PubMed Central for supplementary material.

Acknowledgments

The authors acknowledge members of the Jackson lab, especially Alexander Loktev and Kevin Wright for helpful discussion and careful reading of the manuscript, Keren Hilgendorf for creating RPE-BFP-Cas9 cells and helpful discussion, Ethan Oro for developing the method for measuring the diameter of the ring taken on SIM microscope, and Xin Gu and Jessica Mar for preliminary experiments. The OMX microscope was funded by a NIH High End Instrumentation grant (Dr. Aaron Straight PI), and the project using this microscope was supported, in part, by Award Number 1S10OD01227601 from the National Center for Research Resources (NCRR). Its contents are solely the responsibility of the authors and do not necessarily represent the official views of the NCRR or the National Institutes of Health. This work was support by funds from the Baxter Laboratory for Stem Cell Research, the Stanford Department of Research, the Stanford Cancer Center, NIH grants R01GM114276 and R01GM121565 to PKJ, a grant from the Cell Sciences Imaging Facility of the Beckman Foundation, and postdoctoral support from the Uehara memorial foundation and Human Frontier Science Program to TK.

References

Bangs F, Anderson KV. Primary Cilia and Mammalian Hedgehog Signaling. Cold Spring Harbor perspectives in biology. 2016

Banizs B, Pike MM, Millican CL, Ferguson WB, Komlosi P, Sheetz J, Bell PD, Schwiebert EM, Yoder BK. Dysfunctional cilia lead to altered ependyma and choroid plexus function, and result in the formation of hydrocephalus. Development. 2005; 132:5329–5339. [PubMed: 16284123]

Bhogaraju S, Cajanek L, Fort C, Blisnick T, Weber K, Taschner M, Mizuno N, Lamla S, Bastin P, Nigg EA, et al. Molecular Basis of Tubulin Transport Within the Cilium by IFT74 and IFT81. Science. 2013; 341:1009–1012. [PubMed: 23990561]

Bhogaraju S, Taschner M, Morawetz M, Basquin C, Lorentzen E. Crystal structure of the intraflagellar transport complex 25/27. The EMBO journal. 2011; 30:1907–1918. [PubMed: 21505417]

Bos JL, Rehmann H, Wittinghofer A. GEFs and GAPs: critical elements in the control of small G proteins. Cell. 2007; 129:865–877. [PubMed: 17540168]

Brinkman EK, Chen T, Amendola M, van Steensel B. Easy quantitative assessment of genome editing by sequence trace decomposition. Nucleic acids research. 2014; 42:e168. [PubMed: 25300484]

Brown JM, Cochran DA, Craige B, Kubo T, Witman GB. Assembly of IFT Trains at the Ciliary Base Depends on IFT74. Curr Biol. 2015; 25:1583–1593. [PubMed: 26051893]

Cajanek L, Nigg EA. Cep164 triggers ciliogenesis by recruiting Tau tubulin kinase 2 to the mother centriole. P Natl Acad Sci USA. 2014; 111:E2841–E2850.

Cano DA, Murcia NS, Pazour GJ, Hebrok M. Orpk mouse model of polycystic kidney disease reveals essential role of primary cilia in pancreatic tissue organization. Development. 2004; 131:3457–3467. [PubMed: 15226261]

Cole DG, Diener DR, Himelblau AL, Beech PL, Fuster JC, Rosenbaum JL. Chlamydomonas kinesin-II-dependent intraflagellar transport (IFT): IFT particles contain proteins required for ciliary assembly in Caenorhabditis elegans sensory neurons. The Journal of cell biology. 1998; 141:993–1008. [PubMed: 9585417]

Craft JM, Harris JA, Hyman S, Kner P, Lechtreck KF. Tubulin transport by IFT is upregulated during ciliary growth by a cilium-autonomous mechanism. Journal of Cell Biology. 2015; 208:223–237. [PubMed: 25583998]

Deane JA, Cole DG, Seeley ES, Diener DR, Rosenbaum JL. Localization of intraflagellar transport protein IFT52 identifies basal body transitional fibers as the docking site for IFT particles. Curr Biol. 2001; 11:1586–1590. [PubMed: 11676918]

Dentler W. Intraflagellar transport (IFT) during assembly and disassembly of Chlamydomonas flagella. The Journal of cell biology. 2005; 170:649–659. [PubMed: 16103230]

Diekmann Y, Seixas E, Gouw M, Tavares-Cadete F, Seabra MC, Pereira-Leal JB. Thousands of rab GTPases for the cell biologist. PLoS computational biology. 2011; 7:e1002217. [PubMed: 22022256]

Elias JE, Gygi SP. Target-decoy search strategy for increased confidence in large-scale protein identifications by mass spectrometry. Nature methods. 2007; 4:207–214. [PubMed: 17327847]

Elias M, Klimes V, Derelle R, Petrzelkova R, Tachezy J. A paneukaryotic genomic analysis of the small GTPase RABL2 underscores the significance of recurrent gene loss in eukaryote evolution. Biology direct. 2016; 11:5. [PubMed: 26832778]

Forsythe E, Beales PL. Bardet-Biedl syndrome. Eur J Hum Genet. 2013; 21:8–13. [PubMed: 22713813]

Gasper R, Meyer S, Gotthardt K, Sirajuddin M, Wittinghofer A. It takes two to tango: regulation of G proteins by dimerization. Nat Rev Mol Cell Bio. 2009; 10:423–429. [PubMed: 19424291]

Goetz SC, Anderson KV. The primary cilium: a signalling centre during vertebrate development. Nat Rev Genet. 2010; 11:331–344. [PubMed: 20395968]

Goetz SC, Liem KF Jr, Anderson KV. The spinocerebellar ataxia-associated gene Tau tubulin kinase 2 controls the initiation of ciliogenesis. Cell. 2012; 151:847–858. [PubMed: 23141541]

Ishikawa H, Marshall WF. Ciliogenesis: building the cell's antenna. Nat Rev Mol Cell Bio. 2011; 12:222–234. [PubMed: 21427764]

Jakobsen L, Vanselow K, Skogs M, Toyoda Y, Lundberg E, Poser I, Falkenby LG, Bennetzen M, Westendorf J, Nigg EA, et al. Novel asymmetrically localizing components of human centrosomes identified by complementary proteomics methods. The EMBO journal. 2011; 30:1520–1535. [PubMed: 21399614]

Katoh Y, Michisaka S, Nozaki S, Funabashi T, Hirano T, Takei R, Nakayama K. Practical method for targeted disruption of cilia-related genes by using CRISPR/Cas9-mediated, homology-independent knock-in system. Molecular biology of the cell. 2017; 28:898–906. [PubMed: 28179459]

Kramer M, Backhaus O, Rosenstiel P, Horn D, Klopocki E, Birkenmeier G, Schreiber S, Platzer M, Hampe J, Huse K. Analysis of relative gene dosage and expression differences of the paralogs RABL2A and RABL2B by Pyrosequencing. Gene. 2010; 455:1–7. [PubMed: 20138207]

Kubo T, Brown JM, Bellve K, Craige B, Craft JM, Fogarty K, Lechtreck KF, Witman GB. Together, the IFT81 and IFT74 N-termini form the main module for intraflagellar transport of tubulin. Journal of cell science. 2016; 129:2106–2119. [PubMed: 27068536]

Lee JY, Stearns T. FOP Is a Centriolar Satellite Protein Involved in Ciliogenesis. Plos One. 2013; 8

Lee MT, Mishra A, Lambright DG. Structural mechanisms for regulation of membrane traffic by rab GTPases. Traffic. 2009; 10:1377–1389. [PubMed: 19522756]

Liew GM, Ye F, Nager AR, Murphy JP, Lee JS, Aguiar M, Breslow DK, Gygi SP, Nachury MV. The intraflagellar transport protein IFT27 promotes BBSome exit from cilia through the GTPase ARL6/BBS3. Developmental cell. 2014; 31:265–278. [PubMed: 25443296]

Lo JCY, Jamsai D, O'Connor AE, Borg C, Clark BJ, Whisstock JC, Field MC, Adams V, Ishikawa T, Aitken RJ, et al. RAB-Like 2 Has an Essential Role in Male Fertility, Sperm Intra-Flagellar Transport, and Tail Assembly. Plos Genet. 2012; 8

Martin CL, Wong A, Gross A, Chung J, Fantes JA, Ledbetter DH. The evolutionary origin of human subtelomeric homologies - or where the ends begin. American journal of human genetics. 2002; 70:972–984. [PubMed: 11875757]

Moyer JH, Leetischler MJ, Kwon HY, Schrick JJ, Avner ED, Sweeney WE, Godfrey VL, Cacheiro NLA, Wilkinson JE, Woychik RP. Candidate Gene Associated with a Mutation Causing Recessive Polycystic Kidney-Disease in Mice. Science. 1994; 264:1329–1333. [PubMed: 8191288]

Mukhopadhyay S, Wen X, Ratti N, Loktev A, Rangell L, Scales SJ, Jackson PK. The ciliary G-protein-coupled receptor Gpr161 negatively regulates the Sonic hedgehog pathway via cAMP signaling. Cell. 2013; 152:210–223. [PubMed: 23332756]

Ocbina PJ, Anderson KV. Intraflagellar transport, cilia, and mammalian Hedgehog signaling: analysis in mouse embryonic fibroblasts. Dev Dyn. 2008; 237:2030–2038. [PubMed: 18488998]

Pazour GJ, Baker SA, Deane JA, Cole DG, Dickert BL, Rosenbaum JL, Witman GB, Besharse JC. The intraflagellar transport protein, IFT88, is essential for vertebrate photoreceptor assembly and maintenance. Journal of Cell Biology. 2002; 157:103–113. [PubMed: 11916979]

Pazour GJ, Dickert BL, Vucica Y, Seeley ES, Rosenbaum JL, Witman GB, Cole DG. Chlamydomonas IFT88 and its mouse homologue, polycystic kidney disease gene tg737, are required for assembly of cilia and flagella. The Journal of cell biology. 2000; 151:709–718. [PubMed: 11062270]

Pazour GJ, Dickert BL, Witman GB. The DHC1b (DHC2) isoform of cytoplasmic dynein is required for flagellar assembly. Journal of Cell Biology. 1999; 144:473–481. [PubMed: 9971742]

Pedersen LB, Rosenbaum JL. Intraflagellar transport (IFT) role in ciliary assembly, resorption and signalling. Current topics in developmental biology. 2008; 85:23–61. [PubMed: 19147001]

Pigino G, Geimer S, Lanzavecchia S, Paccagnini E, Cantele F, Diener DR, Rosenbaum JL, Lupetti P. Electron-tomographic analysis of intraflagellar transport particle trains in situ. The Journal of cell biology. 2009; 187:135–148. [PubMed: 19805633]

Rosenbaum JL, Witman GB. Intraflagellar transport. Nature reviews Molecular cell biology. 2002; 3:813–825. [PubMed: 12415299]

Sang L, Miller JJ, Corbit KC, Giles RH, Brauer MJ, Otto EA, Baye LM, Wen X, Scales SJ, Kwong M, et al. Mapping the NPHP-JBTS-MKS protein network reveals ciliopathy disease genes and pathways. Cell. 2011; 145:513–528. [PubMed: 21565611]

Schmidt KN, Kuhns S, Neuner A, Hub B, Zentgraf H, Pereira G. Cep164 mediates vesicular docking to the mother centriole during early steps of ciliogenesis. Journal of Cell Biology. 2012; 199:1083–1101. [PubMed: 23253480]

Shalata A, Ramirez MC, Desnick RJ, Priedigkeit N, Buettner C, Lindtner C, Mahroum M, Abdul-Ghani M, Dong F, Arar N, et al. Morbid obesity resulting from inactivation of the ciliary protein CEP19 in humans and mice. American journal of human genetics. 2013; 93:1061–1071. [PubMed: 24268657]

Shevchenko A, Tomas H, Havlis J, Olsen JV, Mann M. In-gel digestion for mass spectrometric characterization of proteins and proteomes. Nature protocols. 2006; 1:2856–2860. [PubMed: 17406544]

Sloboda RD, Howard L. Localization of EB1, IFT polypeptides, and kinesin-2 in Chlamydomonas flagellar axonemes via immunogold scanning electron microscopy. Cell motility and the cytoskeleton. 2007; 64:446–460. [PubMed: 17326139]

Sonnen KF, Schermelleh L, Leonhardt H, Nigg EA. 3D-structured illumination microscopy provides novel insight into architecture of human centrosomes. Biol Open. 2012; 1:965–976. [PubMed: 23213374]

Stewart SA, Dykxhoorn DM, Palliser D, Mizuno H, Yu EY, An DS, Sabatini DM, Chen IS, Hahn WC, Sharp PA, et al. Lentivirus-delivered stable gene silencing by RNAi in primary cells. Rna. 2003; 9:493–501. [PubMed: 12649500]

Tanos BE, Yang HJ, Soni R, Wang WJ, Macaluso FP, Asara JM, Tsou MF. Centriole distal appendages promote membrane docking, leading to cilia initiation. Genes Dev. 2013; 27:163–168. [PubMed: 23348840]

Taschner M, Kotsis F, Braeuer P, Kuehn EW, Lorentzen E. Crystal structures of IFT70/52 and IFT52/46 provide insight into intraflagellar transport B core complex assembly. Journal of Cell Biology. 2014; 207:269–282. [PubMed: 25349261]

Taschner M, Lorentzen E. The Intraflagellar Transport Machinery. Cold Spring Harbor perspectives in biology. 2016; 8

Taschner M, Weber K, Mourao A, Vetter M, Awasthi M, Stiegler M, Bhogaraju S, Lorentzen E. Intraflagellar transport proteins 172, 80, 57, 54, 38, and 20 form a stable tubulin-binding IFT-B2 complex. Embo Journal. 2016; 35:773–790. [PubMed: 26912722]

Torres JZ, Miller JJ, Jackson PK. High-throughput generation of tagged stable cell lines for proteomic analysis. Proteomics. 2009; 9:2888–2891. [PubMed: 19405035]

Uthaiah RC, Praefcke GJ, Howard JC, Herrmann C. IIGP1, an interferon-gamma-inducible 47-kDa GTPase of the mouse, showing cooperative enzymatic activity and GTP-dependent multimerization. The Journal of biological chemistry. 2003; 278:29336–29343. [PubMed: 12732635]

van Dam TJP, Townsend MJ, Turk M, Schlessinger A, Sali A, Field MC, Huynen MA. Evolution of modular intraflagellar transport from a coatomer-like progenitor. P Natl Acad Sci USA. 2013; 110:6943–6948.

Waters AM, Beales PL. Ciliopathies: an expanding disease spectrum. Pediatric nephrology. 2011; 26:1039–1056. [PubMed: 21210154]

Wong ACC, Shkolny D, Dorman A, Willingham D, Roe BA, McDermid HE. Two novel human RAB genes with near identical sequence each map to a telomere-associated region: The subtelomeric region of 22q13.3 and the ancestral telomere band 2q13. Genomics. 1999; 59:326–334. [PubMed: 10444334]

Wren KN, Craft JM, Tritschler D, Schauer A, Patel DK, Smith EF, Porter ME, Kner P, Lechtreck KF. A Differential Cargo-Loading Model of Ciliary Length Regulation by IFT. Curr Biol. 2013; 23:2463–2471. [PubMed: 24316207]

Wright KJ, Baye LM, Olivier-Mason A, Mukhopadhyay S, Sang LY, Kwong M, Wang WR, Pretorius PR, Sheffield VC, Sengupta P, et al. An ARL3-UNC119-RP2 GTPase cycle targets myristoylated NPHP3 to the primary cilium. Gene Dev. 2011; 25:2347–2360. [PubMed: 22085962]

Yan X, Habedanck R, Nigg EA. A complex of two centrosomal proteins, CAP350 and FOP, cooperates with EB1 in microtubule anchoring. Molecular biology of the cell. 2006; 17:634–644. [PubMed: 16314388]

Yi Lo JC, O'Connor AE, Andrews ZB, Lo C, Tiganis T, Watt MJ, O'Bryan MK. RABL2 Is Required for Hepatic Fatty Acid Homeostasis and Its Dysfunction Leads to Steatosis and a Diabetes-Like State. Endocrinology. 2016; 157:4732–4743. [PubMed: 27732084]

Highlights

- FOP-CEP350 recruits CEP19-RABL2 to the ciliary base to initiate ciliation
- CEP19 captures GTP-bound RABL2, which is activated by intrinsic nucleotide exchange
- RABL2B binds IFT-B as a GTP-specific effector to trigger the entry of IFT
- Rabl2 knockout mice exhibit phenotype characteristic of ciliopathies

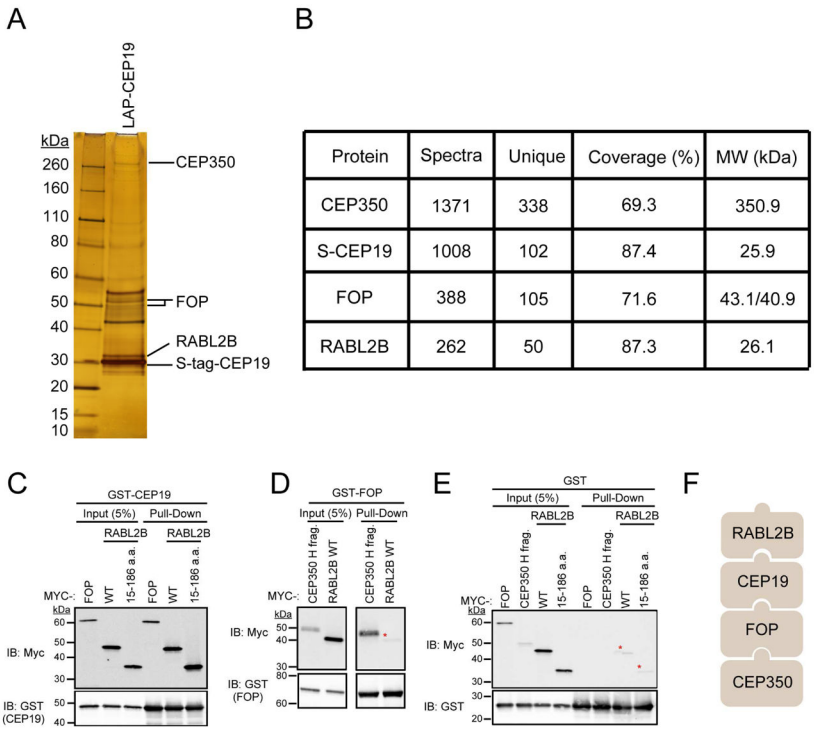

Protein	Spectra	Unique	Coverage (%)	MW (kDa)
CEP350	1371	338	69.3	350.9
S-CEP19	1008	102	87.4	25.9
FOP	388	105	71.6	43.1/40.9
RABL2B	262	50	87.3	26.1

Figure 1. Identification of the centriolar FOP and CEP350 proteins, and of the conserved RABL2B small GTPase as an interactor of CEP19

A–B. (A) Cell lysates from RPE cells expressing N-terminally LAP (EGFP-TEV cleavage site-S tag-PreScission cleavage site)-tagged CEP19 were purified with GFP antibodies and S-protein beads. Proteins were resolved by SDS-PAGE and visualized by silver staining. (B) Spectral counts, unique peptide counts, and coverage indicated in the table.

C–E. GST pull-down assays with indicated purified GST-tagged proteins and IVT MYC-tagged proteins. Eluates analyzed by immunoblotting with indicated antibodies.

Asterisk: Non-specific binding to GST tag.

F. Established order of binding of CEP350, FOP, CEP19, and RABL2B via *in vitro* binding experiments.

See also Figure S1.

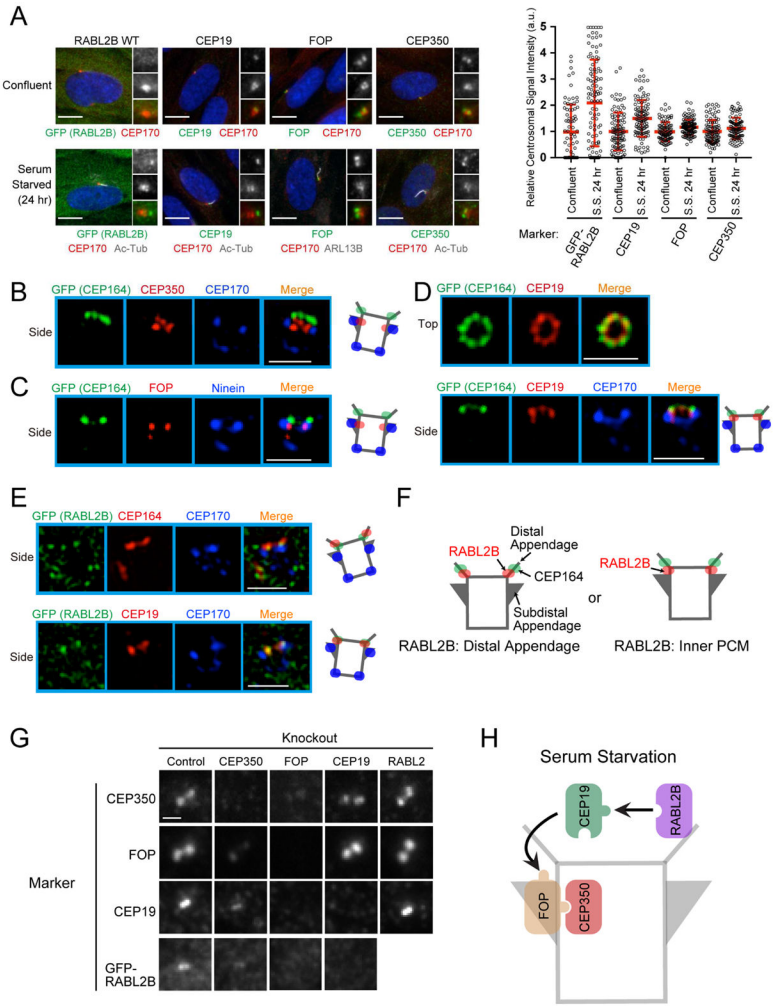

Figure 2. The localization of RABL2B and CEP19 to the inner pericentriolar material is regulated by FOP and CEP350

A. RPE cells or RPE cells expressing GFP-RABL2B were serum starved 24 hr and immunostained with indicated antibodies. The graph (right) shows the normalized fluorescent intensity of the indicated proteins that colocalize with the centrosome in either confluent or 24 hr serum starved (S.S. 24 hr) cells. Scale bar: 10 μm.

B–E. RPE cells expressing GFP-CEP164 (B–D) or GFP-RABL2B (E) were serum starved 24 hr and immunostained with indicated antibodies. Images acquired via structured illumination microscopy. GFP-CEP164: a marker of the distal appendage. CEP170 and Ninein: markers of sub-distal appendage and proximal end of the mother centriole. Scale bar: 1 μm.

F. Alternate hypotheses for RABL2B localization. Top: RABL2B localizes to the proximal region of the distal appendage. Bottom: RABL2B localizes to inner pericentriolar material.

G. RPE-BFP-Cas9 cells with specified gene knockouts were serum starved 24 hr and immunostained with indicated antibodies. Exogenous GFP-RABL2B was expressed in knockout cells and immunostained with α-GFP. Scale bar: 1μm. See Fig. S2C–F for quantification data.

H. The order of recruitment and physical binding for the CEP350-FOP-CEP19-RABL2B pathway.

See also Figure S2.

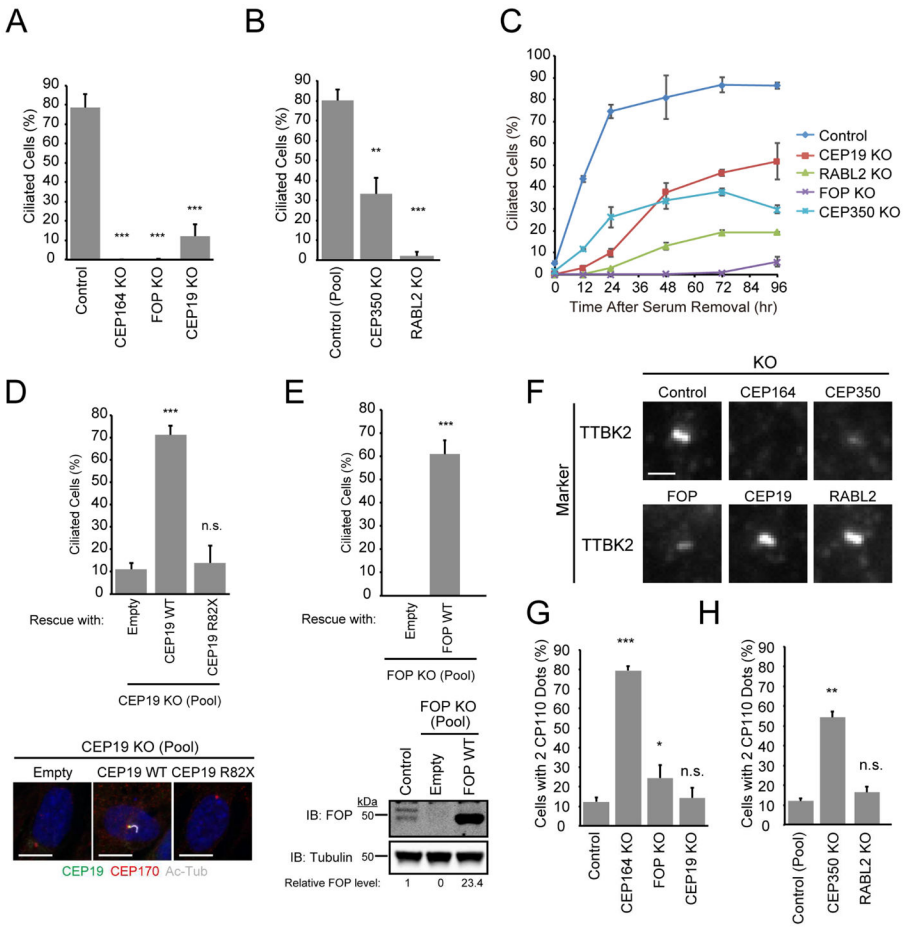

Figure 3. The CEP350/FOP/CEP19/RABL2B complex is important for ciliation

A. Single cell clones (n = 5–6) of RPE-BFP-Cas9 cells with the specified gene knockouts were serum starved 24 hr and subjected to the ciliation assay described in Methods. Data averaged from the indicated number of single cell clones. Error bars represent ± SD. See Fig. S3A for individual clone data.

B. Single cell clones of RPE-BFP-Cas9 cells with the specified gene knockouts were subjected to the ciliation assay. Data averaged from three independent experiments of each clone. Error bars represent ± SD.

C. Pools of RPE-BFP-Cas9 single cell clones with the specified gene knockouts were serum starved for the indicated times, and subjected to the ciliation assay. Data averaged from two independent experiments. Error bars represent ± SD.

D. RPE-BFP-Cas9 CEP19 KO cells stably expressing empty vector, untagged CEP19 WT, or CEP19 R82X were serum starved 24 hr and subjected to the ciliation assay. Top: Ciliation quantification of each cell line. Data averaged from three independent experiments. Scale bar: 10 μm. Error bars represent ± SD. Bottom: Confirmation of CEP19 expression by immunofluorescence.

E. RPE-BFP-Cas9 FOP KO cells stably expressing empty vector or untagged FOP WT were serum starved 24 hr and subjected to the ciliation assay. Top: Ciliation quantification of each cell line. Data averaged from three independent experiments. Error bars represent ± SD.

Bottom: Confirmation of the expression of FOP by immunoblot. Relative expression levels of exogenous compared to endogenous FOP in control RPE cells is indicated.
F. RPE-BFP-Cas9 cells with the specified gene knockouts were serum starved 24 hr and immunostained with α-TTBK2 antibody. Scale bar: 1 μm.
G–H. RPE-BFP-Cas9 cells with the specified gene knockouts were serum starved 24 hr and immunostained with α-CP110 antibody. Data averaged from three single cell clones (G) or three independent experiments (H). Error bars represent ± SD.
See also Figure S3.

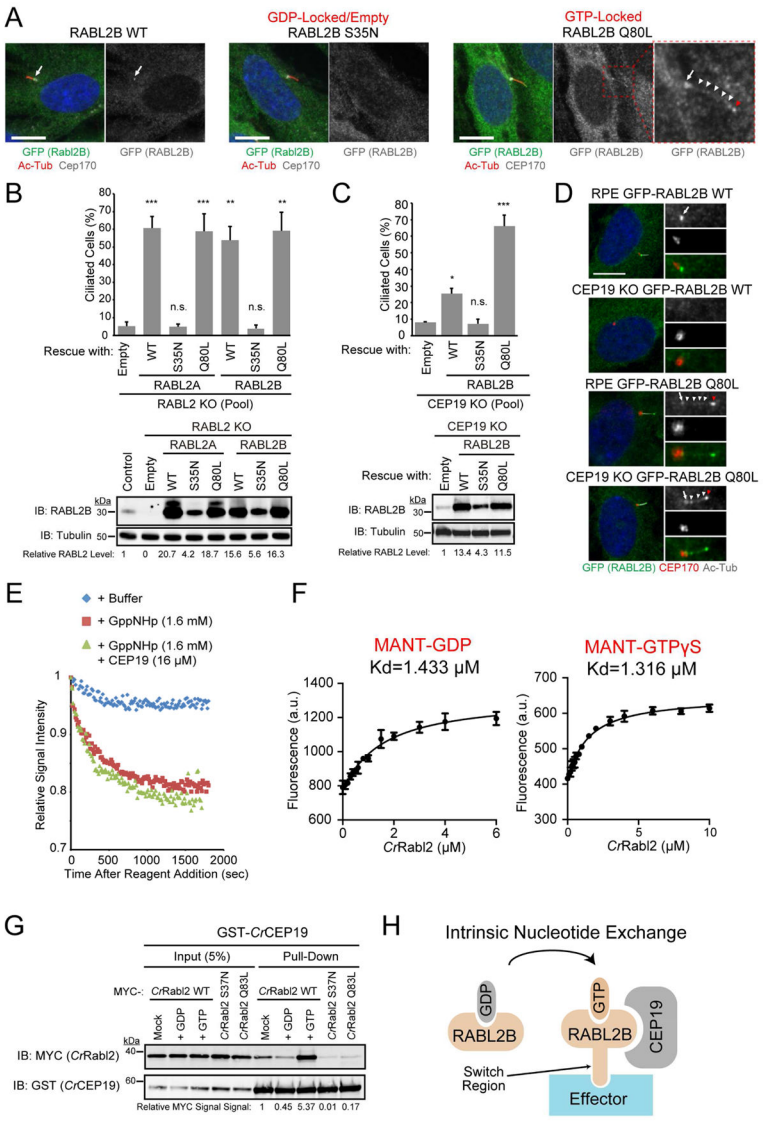

Figure 4. RABL2B is a small GTPase with high intrinsic nucleotide exchange rate

A. RPE cells expressing GFP-RABL2B WT, S35N (GDP-locked/empty), or Q80L (GTP-locked) were serum starved 24 hr and immunostained with indicated antibodies. Arrow: GFP signal at cilium base. Arrowhead: GFP signal within cilium. Red arrowhead: GFP signal at the cilium tip. Scale bar: 10 μm.

B–C. RABL2 or CEP19 KO RPE cells stably expressing empty vector or untagged RABL2A/B WT or mutants were serum starved 24 hr and subjected to the ciliation assay. Top: Ciliation quantification of each cell line. Data averaged from three independent experiments. Error bars represent ± SD. Bottom: Confirmation of RABL2 expression by immunoblot. The relative expression levels of exogenous compared to endogenous RABL2 from control RPE cells is indicated.

D. RPE-BFP-Cas9 or RPE CEP19 knockout cells expressing either GFP-RABL2B WT or Q80L (GTP-locked) were serum starved 24 hr and immunostained with indicated antibodies.

Arrow: GFP signal at cilium base. Arrowhead: GFP signal within cilium. Red arrowhead: GFP signal at the cilium tip. Scale bar: 10 μm.

E. Purified *Cr*Rabl2 was first loaded with MANT-GDP. Nucleotide exchange was initiated by adding buffer (blue), GppNHp (red), or GppNHp and CEP19 (green). Data averaged from four technical replicates. Experiment was performed six times, and one representative is shown.

F. The Kd of *Cr*Rabl2 was determined by measuring the fluorescence increase induced by the titration of *Cr*Rabl2 in 200 nM MANT-GDP (left) or MANT-GTPγS (right). Data averaged from four technical replicates.

G. GST pull-down assay with GST-*Cr*CEP19 and IVT MYC-tagged *Cr*Rabl2 loaded with GDP/GTP, or with *Cr*Rabl2 GDP/GTP-locked mutants. Eluates analyzed by immunoblotting with indicated antibodies.

H. RABL2B intrinsically exchanges GDP for GTP. RABL2B·GTP binds to CEP19 at a site distinct from RABL2B's switch region, which binds to effectors.

See also Figure S4.

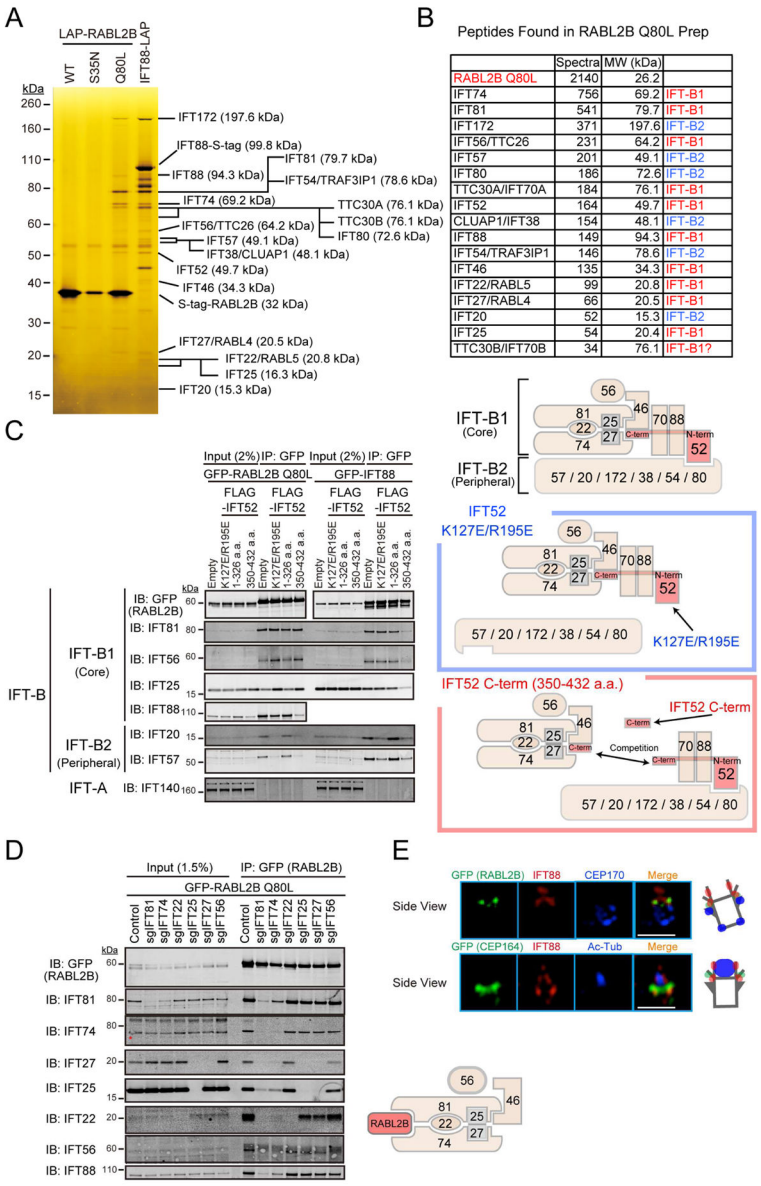

	Spectra	MW (kDa)	
RABL2B Q80L	2140	26.2	
IFT74	756	69.2	IFT-B1
IFT81	541	79.7	IFT-B1
IFT172	371	197.6	IFT-B2
IFT56/TTC26	231	64.2	IFT-B1
IFT57	201	49.1	IFT-B2
IFT80	186	72.6	IFT-B2
TTC30A/IFT70A	184	76.1	IFT-B1
IFT52	164	49.7	IFT-B1
CLUAP1/IFT38	154	48.1	IFT-B2
IFT88	149	94.3	IFT-B1
IFT54/TRAF3IP1	146	78.6	IFT-B2
IFT46	135	34.3	IFT-B1
IFT22/RABL5	99	20.8	IFT-B1
IFT27/RABL4	66	20.5	IFT-B1
IFT20	52	15.3	IFT-B2
IFT25	54	20.4	IFT-B1
TTC30B/IFT70B	34	76.1	IFT-B1?

Figure 5. Identification of the IFT-B complex as an effector of RABL2B

A–B. (A) Cell lysates from RPE cells expressing N-terminally LAP-tagged RABL2B WT or mutants were subjected to tandem affinity purifications as described in Fig. 1A. Cells expressing C-terminally LAP-tagged IFT88 serve as a comparison for comparing the migration of individual IFT-B subunits. (B) Spectral counts indicated in the table.

C. Dissociation of the IFT-B complex via expression of the dominant-negative IFT52 allowed identification of the subcomplex that interacts with RABL2B. Left: RPE cells stably expressing N-terminally GFP-tagged RABL2B Q80L (GTP locked form) or C-terminally GFP-tagged IFT88 and indicated N-terminally FLAG-tagged IFT52 mutants were serum starved 24 hr and immunoprecipitated with α-GFP antibody. Eluates analyzed by immunoblotting with indicated antibodies. Right: A cartoon depicting the dissociation of IFT-B by IFT52 mutant expression. IFT52 K127E/R195E dissociates IFT-B into the IFT-B1

and IFT-B2 sub-complexes. The C-terminal fragment (350–432 a.a.) of IFT-52 dissociates the IFT81/74/22/27/25/46/56 sub-complex from the IFT-B holocomplex. The N-terminal fragment (1-326 a.a.) of IFT52 fails to dissociate IFT-B.

D. The individual components of the IFT81/74/22/25/27/56 sub-complex were deleted to determine the direct interactor of RABL2. Left: RPE cells with the specified sgRNAs were infected with lentivirus carrying GFP-RABL2B Q80L (GTP-locked). Cells were serum starved 24 hr and immunoprecipitated with α-GFP antibody. Eluates analyzed by immunoblotting with indicated antibodies. Asterisk: Non-specific band masking endogenous IFT74. Right: A cartoon depicting the interaction of RABL2B and IFT-B.

E. RPE cells expressing GFP-CEP164 or GFP-RABL2B were serum starved 24 hr and immunostained with the indicated antibodies. Images acquired via structured illumination microscopy. Scale bar: 1 μm.

See also Figure S5 and Table S1.

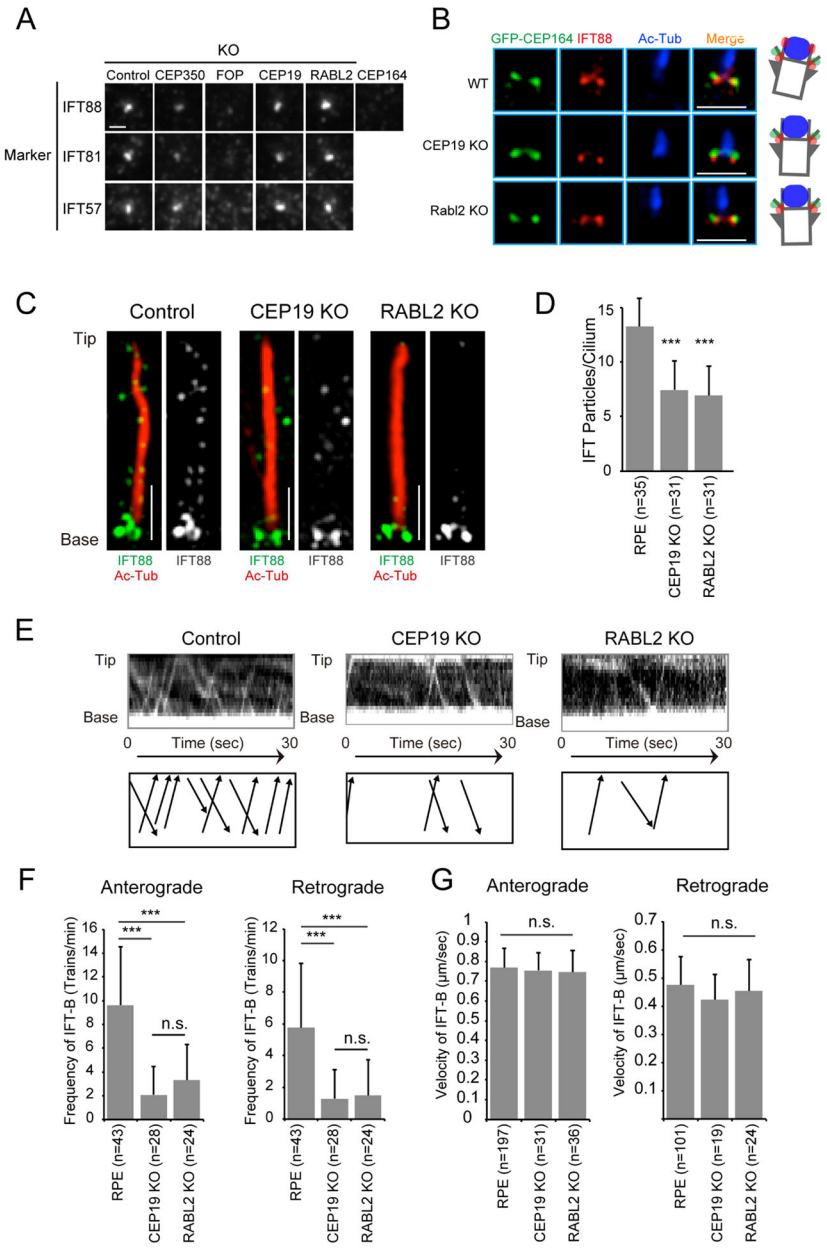

Figure 6. RABL2B triggers the entry of IFT-B into the cilium

A. RPE-BFP-Cas9 and the specified knockout cells were serum starved 24 hr and immunostained with indicated antibodies. Scale bar: 1 μm. See Fig. S6F–H for quantification data.

B. RPE-BFP-Cas9, CEP19 KO, and RABL2 KO cells expressing GFP-CEP164 were serum starved 24 hr and immunostained with indicated antibodies. Images acquired via structured illumination microscopy. Scale bar: 1 μm.

C–D. (C) RPE-BFP-Cas9, CEP19 KO, and RABL2 KO cells were serum starved 48 hr and immunostained with indicated antibodies. Images acquired via structured illumination microscopy. (D) Quantification of IFT-B particles described in (C). Error bars represent ± SD. Scale bar: 1 μm.

E. RPE-BFP-Cas9, CEP19 KO, and RABL2 KO cells expressing C-terminally GFP-tagged IFT80 were serum starved 48 hr and live-cell imaged via TIRF microscopy. Top: Kymographs created from live-cell microscopy movie S1. Bottom: The movement of IFT-B trains interpreted from the kymographs. See Movie S1.

F–G. Quantification of the frequency (F) and velocity (G) of IFT-B trains. Sample size represents the number of cilia (F) or particles (G) analyzed.

See also Figure S6 and Movie S1.

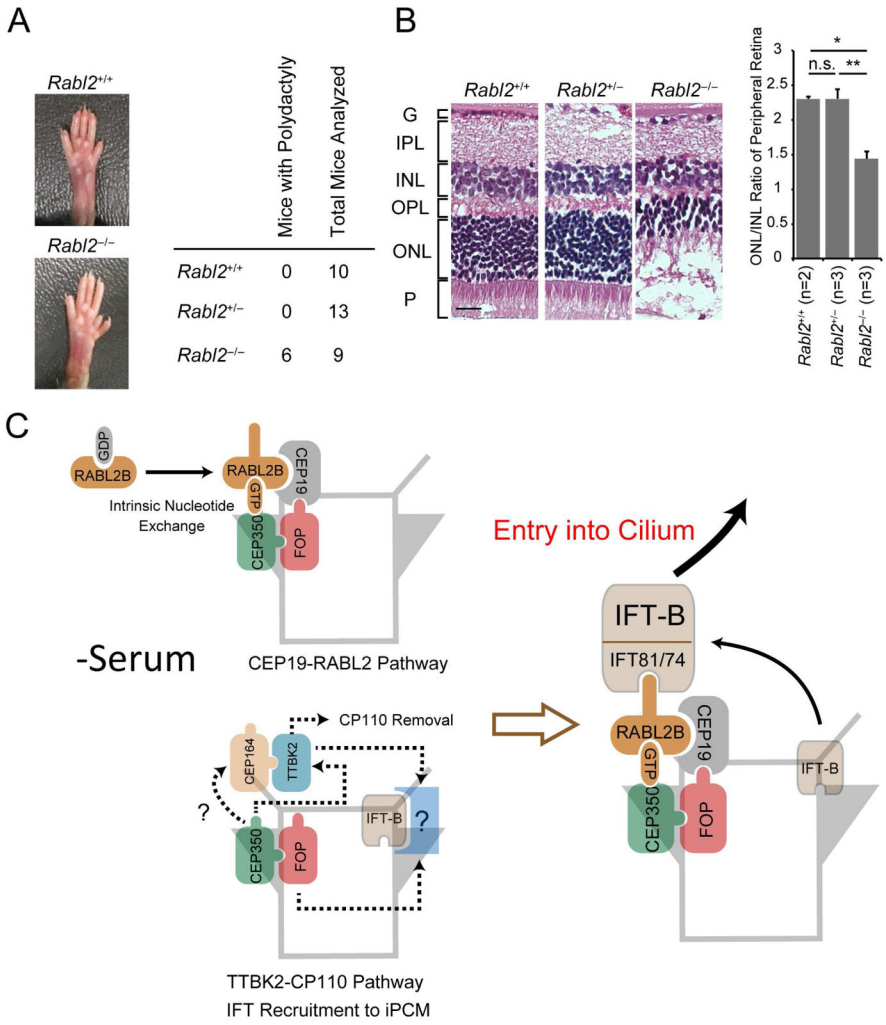

Figure 7. Histological analysis of key tissues supports a BBS-like phenotype for Rabl2 knockouts

A. Left: A representative image of the right hind limb from Rabl2$^{-/-}$ mice with polydactyly. Right: Quantification of the proportion of mice with polydactyly.

B. Left: Histological analysis of the retina from 16-week-old mice. G, ganglion cell layer; IPL, inner plexiform layer; INL, inner nuclear layer; OPL, outer plexiform layer; ONL, outer nuclear layer; P, photoreceptor cell layer. Scale bar: 20 μm. Right: Quantification of ONL/INL ratio of peripheral retina. Error bars represent ± SD.

C. A model for the mechanism by which RABL2B triggers the entry of IFT-B into the cilium.

Table 1

The diameters of the CEP350, FOP, CEP19, and RABL2B rings at the mother centriole

Protein	Diameter (nm)	No. Analyzed Centrioles	Localization
GFP-CEP164	449.0 ± 35.0	13	Distal Appendage
CEP164	433.3 ± 26.7	16	Distal Appendage
CEP350 (Mother centriole)	387.0 ± 21.9	11	Inner Pericentriolar Material
FOP (Mother centriole)	380.0 ± 19.0	11	This Paper
CEP19	372.6 ± 16.4	15	This Paper
GFP-RABL2B	376.5 ± 31.3	10	This Paper

The diameters of the CEP350, FOP, CEP19, and RABL2B rings were significantly different from that of the CEP164 ring ($p < 0.001$).

The diameters of the FOP, CEP19, and RABL2B rings were similar to that of the CEP350 ring ($p = 0.4539$, One-Way ANOVA).